J. Fluid Mech. (2010), *vol.* 665, *pp.* 1–45. © Cambridge University Press 2010
doi:10.1017/S0022112010003769

A numerical investigation of fine particle laden flow in an oscillatory channel: the role of particle-induced density stratification

CELALETTIN E. OZDEMIR[1]†, TIAN-JIAN HSU[2] AND S. BALACHANDAR[3]

[1]Civil and Coastal Engineering, University of Florida, Gainesville, FL 32611, USA

[2]Civil and Environmental Engineering, Center for Applied Coastal Research, University of Delaware, Newark, DE 19716, USA

[3]Mechanical and Aerospace Engineering, University of Florida, Gainesville, FL 32611, USA

(Received 21 January 2010; revised 9 July 2010; accepted 11 July 2010)

Studying particle-laden oscillatory channel flow constitutes an important step towards understanding practical application. This study aims to take a step forward in our understanding of the role of turbulence on fine-particle transport in an oscillatory channel and the back effect of fine particles on turbulence modulation using an Eulerian–Eulerian framework. In particular, simulations presented in this study are selected to investigate wave-induced fine sediment transport processes in a typical coastal setting. Our modelling framework is based on a simplified two-way coupled formulation that is accurate for particles of small Stokes number (St). As a first step, the instantaneous particle velocity is calculated as the superposition of the local fluid velocity and the particle settling velocity while the higher-order particle inertia effect neglected. Correspondingly, only the modulation of carrier flow is due to particle-induced density stratification quantified by the bulk Richardson number, Ri. In this paper, we fixed the Reynolds number to be $Re_{\Delta} = 1000$ and varied the bulk Richardson number over a range ($Ri = 0$, 1×10^{-4}, 3×10^{-4} and 6×10^{-4}). The simulation results reveal critical processes due to different degrees of the particle–turbulence interaction. Essentially, four different regimes of particle transport for the given Re_{Δ} are observed: (i) the regime where virtually no turbulence modulation in the case of very dilute condition, i.e. $Ri \sim 0$; (ii) slightly modified regime where slight turbulence attenuation is observed near the top of the oscillatory boundary layer. However, in this regime a significant change can be observed in the concentration profile with the formation of a lutocline; (iii) regime where flow laminarization occurs during the peak flow, followed by shear instability during the flow reversal. A significant reduction in the oscillatory boundary layer thickness is also observed; (iv) complete laminarization due to strong particle-induced stable density stratification.

Key words: particle/fluid flows, sediment transport, stratified flows

† Email address for correspondence: eozdemir@ufl.edu

1. Introduction

Particle transport in an oscillatory channel has been a topic of interest in many disciplines of research. Particle transport and deposition through respiratory airways (Nowak, Kakade & Annapragada 2003), blood transport in arteries (Taylor 1959) and sediment transport driven by waves and currents are a few example applications in biomedical and coastal engineering. Wave-induced fine-sediment transport is one of the major mechanisms shaping the coastal morphodynamics and has a considerable impact on the fate of terrestrial sediment in the coastal ocean (e.g. Traykovski *et al.* 2000; Harris, Traykovski & Geyer 2005). Motivated by this application, we aim to improve our current understanding of the wave-induced turbulence and its interaction with the fine-sediment transport.

Wave-resolving Reynolds-averaged two-phase models are available for studying the effect of the wave-induced sediment transport. The effects of the turbulence–particle interaction (i.e. two-way coupling, Conley *et al.* 2008; Hsu, Ozdemir & Traykovski 2009) and the particle–particle interaction (four-way coupling, Hsu, Jenkins & Liu 2004; Yu, Hsu & Hanes 2010) have been investigated. However, Reynolds-averaged models suffer from uncertainties in turbulence closure. For example, semi-empirical parameters are used in the transport equations and critical assumptions, such as eddy viscosity, isotropy and similarity relationships are used in the standard two-equation models. These closure issues become more problematic due to the unsteady nature of oscillatory flow and intense particle–turbulence interactions. Hence, the underlying assumptions of Reynolds-averaged closures need to be tested against simulations where turbulence is fully resolved. On the other hand, existing fully resolved direct numerical simulation (DNS) studies (Spalart & Baldwin 1989; Vittori & Verzicco 1998; Salon, Armenio & Crise 2007) investigate oscillatory boundary layer without particles. Scotti & Piomelli (2001) adopted large-eddy simulation (LES) for the investigation of pulsating flow in a channel at a higher Reynolds number. More recently, Salon *et al.* (2007) carried out inter-comparison between LES and DNS at Reynolds number (Re_{Δ}) = 990 (see (1.1)) and LES at Re_{Δ} as high as 1790. The study of Chang & Scotti (2006) utilizes LES for particle-laden oscillatory boundary layer with particle phase assumed to be completely passive to carrier turbulent flow. As discussed in this paper, assuming particles to be completely passive is valid only under an extremely dilute condition. Even at a low concentration where particle–particle interaction can be ignored, the back effect of suspended particles on the carrier phase can be significant. In particular, the magnitude of the carrier-phase turbulence is modulated and the nature of two-phase flow turbulence, such as the degree of isotropy and kinetic energy budget, is altered. This change in the carrier-phase turbulence in turn influences the resulting particle suspension/deposition processes in an oscillatory flow.

Despite pioneering studies of turbulence modulation by experiments (Rogers & Eaton 1991; Tanaka & Eaton 2008), point particle simulations (Maxey 1987; McLaughlin 1989; Elghobashi 1991; Squires & Eaton 1991; Elghobashi & Trusdell 1992, 1993) and fully resolved simulations (Bagchi & Balachandar 2003, 2004; Burton & Eaton 2005; Zeng *et al.* 2008; Zeng, Balachandar & Najjar 2010), our understanding remains incomplete. In general, it is observed that small neutrally buoyant particles at low concentrations tend to suppress turbulence, while larger particles contribute to turbulence enhancement. There are several mechanisms that contribute to the modulation of the carrier-phase turbulence. Added inertia of the suspended particles, increased dissipation due to hydrodynamic drag on the particles and enhanced effective viscosity of the suspension are three mechanisms that

contribute to the suppression of the carrier-phase turbulence. On the other hand, if the particle Reynolds number is sufficiently large, carrier-phase turbulence can be augmented through wake oscillation and vortex shedding. Finally, local vertical variations in particle concentration can introduce stable or unstable stratification and contribute to turbulence modulation (e.g. Huppert, Turner & Hallworth 1995; see Balachandar & Eaton 2010 for a more complete review). Here we consider a sufficiently dilute transport of fine particles that the particle inertial, enhanced viscosity and vortex shedding effects are unimportant. Our focus is on the last mechanism where the effect of particle-induced density stratification on the carrier flow turbulence is of critical interest.

In the case of fine particles (or floc aggregate) in water, their relative negative buoyancy results in gravitational settling towards the bottom. Turbulence near the bottom boundary contributes to resuspension of particles and an effective (turbulent) diffusion of particles away from the bottom. In a statistically stationary flow, the above two mechanisms statistically balance each other and determine the vertical variation of mean particle concentration and the degree of stable density stratification. The earlier studies addressing this problem are carried out by Vanoni (1946) and Einstein & Chien (1955). Both these experimental works concluded that the change in the Reynolds-averaged mean velocity is due to suspended particles, and the modified mean velocity profile can be parameterized in terms of a reduced value of the von Karman constant. More importantly, Vanoni (1946) hypothesized that particle-induced stable density stratification is responsible for the decrease in turbulence, which in turn contributed to the modification of the mean velocity. Later studies account for the effect of particle-induced stable density stratification using different parameterizations. Gelfenbaum & Smith (1986) proposed a reduction factor for eddy viscosity as a function of the Richardson number. Hino (1963) and Zhou & Ni (1995) evaluated changes to the von Karman constant in terms of particle concentration. Turner (1973) and Barenblatt (1953) adopted damping functions for eddy viscosity as a function of the Monin–Obukhov length scale. The numerical study by Noh & Fernando (1991) utilized one-equation closure incorporating the effect of particles on turbulent flow due to density stratification to model particle suspension by an oscillating grid and the formation of lutocline. More recent numerical study by Winterwerp (2001, 2002), Hsu, Traykovski & Kineke (2007), Hsu *et al.* (2009) adopt two-way coupled two-equation turbulence closures for the fine-sediment transport in the tidal boundary layer and the wave-current boundary layer, respectively.

The unsteady nature of the oscillatory particulate flow presents a challenge compared with steady flow or tidal variations. Under ideal sinusoidal forcing, the flow velocity varies between positive and negative peaks with flow reversal in between. If the instantaneous flow velocity becomes sufficiently large, then perturbations in the flow start to grow during the acceleration phase, and depending upon the extent of the acceleration phase, the flow might become fully turbulent. During deceleration, the grown perturbations may fully decay and the flow might laminarize. Or depending on the maximum velocity that the flow reaches, the perturbations may only partially decay and the flow can remain turbulent throughout the entire oscillatory cycle. This unsteady nature of the flow has motivated researches to address the onset of turbulence (Hino, Sawamoto & Takasu 1976) and the evolution of vortex structures (Sarpkaya 1993). These studies have classified four flow regimes based on the Reynolds number defined: (i) laminar regime ($Re_\Delta < 200$), (ii) disturbed laminar regime ($200 < Re_\Delta < 400$), (iii) intermittently turbulent regime ($400 < Re_\Delta < 1200$), and (iv) fully turbulent regime ($Re_\Delta > 1200$). The Reynolds number Re_Δ is defined

as

$$Re_{\Delta} = \frac{\tilde{U}_0 \tilde{\Delta}}{\nu_f}, \tag{1.1}$$

where $\tilde{U}_0$ is the dimensional maximum free-stream velocity, $\tilde{\Delta}$ is the dimensional Stokes boundary-layer thickness defined as $\tilde{\Delta} = \sqrt{2\nu_f/\tilde{\omega}}$ with $\tilde{\omega}$ being the dimensional angular frequency of oscillatory forcing, and ν_f is the kinematic viscosity of the fluid. Alternatively, in many coastal sediment transport studies, the Reynolds number is defined using the orbital semi-excursion length, $\tilde{a} = \tilde{U}_0/\tilde{\omega}$ (see for example Jehnsen, Sumer & Fredsóe 1989):

$$Re_a = \frac{\tilde{U}_0 \tilde{a}}{\nu_f}. \tag{1.2}$$

After algebraic manipulation the relation between these two Reynolds numbers defined in (1.1) and (1.2) is obtained as follows:

$$Re_a = \frac{Re_{\Delta}^2}{2}. \tag{1.3}$$

In the laminar regime, the flow stays laminar over the entire wave cycle, and in the fully turbulent regime it stays turbulent throughout the wave cycle. In the perturbed laminar regime, the flow is perturbed during the acceleration phase and laminarizes during the deceleration without ever becoming fully turbulent. Finally, in the intermittently turbulent regime, the flow becomes turbulent starting from the late acceleration phase and tends to decay during the late deceleration phase without complete laminarization. The signature characteristic of the intermittently turbulent regime is the formation of bursts at the late stages of deceleration (Hino *et al.* 1983; Salon *et al.* 2007; Ozdemir, Hsu & Balachandar 2010). This burst phenomenon is very important for suspension/deposition of particles and is therefore revisited in § 3.2.

DNS of the oscillatory channel flow in a clear fluid was initiated by Spalart & Baldwin (1989) and continued in by Akhavan, Kamm & Shapiro (1991), Vittori & Verzicco (1998) and Costamagna, Vittori & Blondeaux (2003). Recently, Ozdemir *et al.* (2010) performed numerical simulations in the intermittently turbulent regime for a very dilute particle concentration, where particles can be assumed to be passive and do not influence the carrier flow. They used a higher-order accurate pseudo-spectral flow solver and employed the same domain size and resolution as Spalart & Baldwin (1989) did. These simulations are of high fidelity since they use a large computational domain, a fine grid resolution and a spectrally accurate numerical methodology. Ozdemir *et al.* (2010) observe randomly distributed energetic vortices present at the maximum free-stream velocity. These vortices start to lose their energy during the flow reversal and are uplifted towards the upper portions of the channel, where they manifest themselves as random spikes in decelerating phases shown in concentration and vorticity iso-contours. These vortices then transform into organized long streaks at the early stages of acceleration. Correspondingly, the peak turbulent fluctuation occurs close to the bottom boundary when free-stream velocity reaches its maximum. Then, turbulent intensity reduces and the peak shifts away from the bottom boundary.

The two-way coupled effects between sedimenting particles and carrier flow turbulence were investigated by Cantero *et al.* (2009*b*) in the context of a fully turbulent turbidity current. They used a current-with-a-roof model to consider the statistically stationary state. Their simulation results revealed a decrease in the turbulent intensity with increasing particle-induced stratification effect, and the variation

in the effective von Karman constant is revisited. Most importantly, it was observed that at a specified particle concentration (correspondingly, a fixed Richardson number), above a threshold particle settling velocity, the stratification effect becomes strong enough to kill turbulence and the flow relaminarizes. Under such condition the particles cannot be kept in suspension and massive deposition from the turbidity current occurs.

The problem of turbulence modulation by particles in an oscillatory flow is far more challenging. As discussed above, even in the limit of a clear fluid, depending on the Reynolds number, turbulence may be limited to only part of the wave cycle. Correspondingly, the interaction between suspended particles and carrier flow turbulence can be complex and highly variable over the wave cycle. In this study, we shall investigate the following issues of fine-particle transport in an oscillatory boundary layer using two-way coupled numerical simulations and discuss their relevance to existing field and laboratory observations: (i) The formation of sharp stable particle concentration gradient, i.e. lutocline, in an oscillatory boundary layer; (ii) the observation of instability and bursting events during the flow reversal and early decelerating phases in a stratified turbulent flow; and (iii) complete laminarization due to particle-induced stratification.

The mathematical formulation of fine-particles transport in the oscillatory channel flow is discussed in detail in § 2. The Reynolds number in this study is selected to be $Re_\Delta = 1000$ (i.e. $Re_a = 5 \times 10^5$), which is a plausible value under wave conditions observed during fluid mud events at continental shelf (to be discussed below). On the basis of this Reynolds number, the non-dimensional particle settling velocity is chosen to be consistent with typical observed fine-sediment settling velocity. Four simulations are carried out for a range of bulk Richardson number ($Ri = 0,\ 1 \times 10^{-4},\ 3 \times 10^{-4}$ and 6×10^{-4}), which covers the entire range of fully developed turbulence to complete relaminarization. Section 3 is devoted to a detailed analysis of the simulation results in terms of turbulent structure, mean flow and turbulence statistics, suspension and deposition processes, and turbulent kinetic energy budget. In § 4, we discuss observed flow regimes and their relevance to existing field/laboratory observations of fine-sediment transport in a wave boundary layer. In § 5, we present conclusions and recommendations for the future work.

2. Mathematical formulation

In this study, we closely follow the mathematical model adopted in the particulate gravity (Harris, Hogg & Huppert 2001; Necker *et al.* 2002) and turbidity current research (Felix 2002; Hall, Meiburg & Kneller 2008; Cantero *et al.* 2009*a*; Sequeiros *et al.* 2009), where mixing and transport characteristics of the dispersed phase in a two-phase flow context are similar to our problem. As mentioned in § 1, we present four different cases over a range of Ri to identify the effect of particle concentration on the carrier-phase turbulence and particle transport mechanisms. With this motivation, we keep other non-dimensional parameters constant, i.e. the Reynolds number, Re_Δ, and the non-dimensional settling velocity V_s are held fixed. A wide range of dimensional flow and particle parameters, such as particle size, flow velocity amplitude and wave period, satisfy the selected combination of Re_Δ, V_s and Ri. The realistic range of particle and flow variables that are observed in a typical marine environment falls within the selected non-dimensional parameters. This can be exemplified in a typical coastal settling as follows: surface waves at continental shelf have a wave period of about 10 s and the corresponding Stokes boundary layer thickness is $\tilde{\Delta} = 1.8 \times 10^{-3}$ m.

Here, a Reynolds number (see (1.1)) of $Re_\Delta = 1000$ (or $Re_a = 5 \times 10^5$) corresponds to an oscillatory flow velocity amplitude of 0.56 m s^{-1}. This value is similar in magnitude to that observed at a continental shelf where fluid mud is suspended in the wave boundary layer (e.g. Traykovski, Wieberg & Geyer 2007; Traykovski *et al.* 2000). We consider a suspension of fine silt in marine environment. Typical silt size of 24×10^{-6} m (=24 μm) with a specific gravity of 2.65 results in a still fluid settling velocity of about 0.5×10^{-3} m s^{-1}. The particle time scale, defined as $\rho_p d^2/18\mu_f$, can be computed to be 8.5×10^{-5} s, where ρ_p is the particle density, d is the particle diameter and μ_f is the dynamic viscosity of water. The time scale of the Stokes layer ($\tilde{\Delta}/\tilde{U}_0$) can be calculated as 3.2×10^{-3} s. Hence, the non-dimensional particle response time is only 0.0264.

For the current case of $Re_\Delta = 1000$, as shown below, the flow is turbulent provided the back effect of the suspended particles is small. The flow thus presents a range of time scales from the integral to the Kolmogorov scale. The Kolmogorov time scale $\tilde{\tau}_l$ can be calculated as follows:

$$\tilde{\tau}_l = (\tilde{\varepsilon}/\nu_f)^{-1/2}, \tag{2.1}$$

where $\tilde{\varepsilon}$ is the dimensional turbulent dissipation rate. Hence, the non-dimensional Kolmogorov time scale can be written as

$$\tau_l = (Re_\Delta\, \varepsilon)^{-1/2}. \tag{2.2}$$

We can see that as the turbulent dissipation rate increases, the non-dimensional Kolmogorov time scale τ_l decreases and the Stokes number based on the Kolmogorov time scale (τ_p/τ_l) increases. Therefore, the use of the maximum dissipation rate ε_{max} within the wave cycle of the passive simulation, where there is no turbulence decay, allows us to estimate the most conservative Stokes number, St. The turbulent kinetic energy (TKE) budget in the passive case without the particles gives a maximum non-dimensional ε of 0.0016 (see figure 19). This gives a non-dimensional Kolmogorov time scale of 0.791. Hence, in this study, the particle Stokes number based on the Kolmogorov time scale is no more than 0.033, and is often far smaller. It can thus be established that for this study, particles are sufficiently small that their Stokes number is far less than 1. As a result, we simply define the non-dimensional particle velocity U_i^P as the sum of the fluid velocity U_i^f and the particle settling velocity V_s as

$$U_i^p = U_i^f + V_s \delta_{i2}, \tag{2.3}$$

where the superscripts f and p stand for the fluid and particle phases, respectively. Substituting the above algebraic relationship in the Eulerian–Eulerian two-phase equations and applying the Boussinesq approximation, which is valid for relatively small concentrations, the resulting governing equations can be greatly simplified (e.g. Cantero, Balachandar & Garcia 2008). The continuity (2.4) and momentum equations (2.5) of the fluid–particle mixture can be written as

$$\nabla \cdot \boldsymbol{U}^f = 0, \tag{2.4}$$

$$\frac{\mathrm{D}\boldsymbol{U}^f}{\mathrm{D}t} = -\frac{2}{Re_\Delta} \cos\left(\frac{2}{Re_\Delta} t\right) \boldsymbol{e}_1 - \nabla P' - Ri\, C \boldsymbol{e}_2 + \frac{1}{Re_\Delta} \nabla^2(\boldsymbol{U}^f). \tag{2.5}$$

These equations are non-dimensionalized by length, velocity and time scales selected to be the Stokes boundary layer thickness ($\tilde{\Delta}$), maximum free-stream velocity ($\tilde{U}_0$) and $\tilde{\Delta}/\tilde{U}_0$, respectively. Note that $\boldsymbol{e}_1$ and $\boldsymbol{e}_2$ correspond to unit vectors along the streamwise and wall-normal directions, respectively. Note that the particle volume concentration

considered in this study is sufficiently dilute, i.e. $O(0.01)$, and since the particle-to-fluid density ratio is $O(1)$ the density variations in the flow can be considered small. Hence, the Boussinesq approximation is appropriate and furthermore makes it possible to impose incompressibility in the continuity equation.

In this problem of an oscillatory channel flow, the time variation of the dimensional free-stream velocity is given as follows:

$$\tilde{\boldsymbol{U}} = \tilde{U}_0 \cos(\tilde{\omega}\tilde{t})\, \boldsymbol{e}_1. \tag{2.6}$$

Far from the bottom boundary, well outside the oscillatory boundary layer, the momentum equation can be simplified for the inviscid flow to yield the mean streamwise pressure gradient to be

$$\frac{\partial \tilde{P}}{\partial \tilde{x}} = -\rho_f\, \tilde{U}_0 \tilde{\omega} \sin(\tilde{\omega}\tilde{t}). \tag{2.7}$$

The above equation upon non-dimensionalization, along with the definition of the Stokes layer thickness and Reynolds number, reduces to the first term on the right-hand side of (2.5). The second term corresponds to the fluctuating pressure gradient. The third term on the right-hand side represents the back effect of the particle on the fluid phase via particle-induced density stratification, which is only effective in the vertical direction. Here, the bulk Richardson number, Ri, is defined as

$$Ri = \frac{(\rho_p - \rho_f) g \tilde{\Delta}}{\rho_f \tilde{U}_0^2} \bar{\tilde{C}}, \tag{2.8}$$

where ρ_f is the fluid density and $\bar{\tilde{C}}$ is the volume-averaged concentration over the entire computational domain, i.e.

$$\bar{\tilde{C}} = \frac{\int \tilde{C}(x, y, z) d\forall}{\forall}. \tag{2.9}$$

Here, $\forall$ is the volume of the domain. In the present formulation, concentration is normalized by $\bar{\tilde{C}}$. As the particles settle within the fluid, their back-coupling on the fluid per unit volume is given by the force $\tilde{C}\rho_p \boldsymbol{g}$, where $\boldsymbol{g}$ is the gravitational acceleration and $\tilde{C}$ is the non-normalized particle concentration. If combined with the gravitational force on the fluid phase, $(1 - \tilde{C})\rho_f \boldsymbol{g}$, and upon non-dimensionalization, we obtain the third term in the momentum equation (2.5). This level of two-way coupling is consistent with the assumption shown in (2.3) that particle velocity is a superposition of the local fluid velocity and particle settling velocity. This formulation does not account for the inertial effect of particles on particle motion and hence processes such as preferential accumulation are not expected in our simulations, which is appropriate for the present particles of a very small St. Also, correspondingly, correction to the frictional or drag force arising from particle inertia is neglected in the momentum equation.

Finally, the particle concentration is calculated by the conservation of particle mass:

$$\frac{\partial}{\partial t}(C) + \nabla \cdot [(\boldsymbol{U}^f + V_s \boldsymbol{e}_2) C] = \frac{1}{Re_\Delta\, Sc} \nabla^2 C. \tag{2.10}$$

The term on the right-hand side represents an effective diffusive flux. Here, the Schmidt number is $Sc = \nu_f/\kappa$, where κ is the effective diffusivity of the particles. The governing equation of particle motion, when applied in the Lagrangian framework, contains no diffusive effect, i.e. $Sc \to \infty$. However, in the literature of

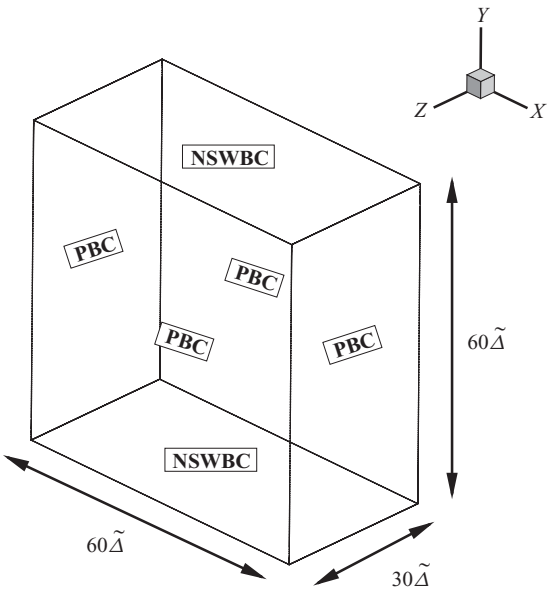

FIGURE 1. Schematic of the computational domain used in the present simulations. No-slip wall boundary condition (NSWBC) is imposed at the top and bottom planes, and periodic boundary condition (PBC) is imposed on the streamwise and spanwise ends of the domain. The size of the computational domain is 60, 30 and 60 times the Stokes boundary layer thickness along the streamwise, spanwise and wall-normal directions, respectively.

Eulerian–Eulerian simulations of particle-laden gravity and turbidity currents, a diffusion term is invariably present (Necker *et al.* 2002; Cantero *et al.* 2009*a*; Sequerios *et al.* 2009). The rationale of adding particle diffusion term is to account for the subgrid-scale random motion of particles due to their interaction, which yields a net particle flux. Following prior simulations, in the present simulations as well a diffusive term is required not only for numerical stability but also to account for the sub-scale particle flux. Birman, Martin & Meiburg (2005) show that the effect of Sc within the range of (0.2, 5.0) is quite insensitive in moderately energetic gravity flows. Similarly, Bonometti & Balachandar (2008) have investigated the effect of Sc in the range of $[1, \infty)$ for gravity currents with similar governing equations, and observed that the Schmidt number effect is small in high-Reynolds-number flows. It is observed that in vigorous flows, mixing is dominated by advection and the effect of molecular mixing represented by diffusion is quite small. We have selected Sc to be 0.5 in these simulations.

The velocity boundary conditions at both the top and bottom boundaries are no-slip wall boundary conditions. Periodic boundary conditions are imposed at the lateral boundaries of the computational domain for both the velocity and the particle concentration (see figure 1). For the particle concentration, the following relation is imposed at both the top and bottom boundaries of the computational domain:

$$V_s \frac{\partial C}{\partial y} = \frac{1}{Re_\Delta \, Sc} \frac{\partial^2 C}{\partial y^2}. \tag{2.11}$$

This boundary condition imposes no net transport of particles across the top and bottom boundaries. These boundary conditions in turn imply that the total volume of

particles remains constant in the domain throughout the computation. This integral property has been confirmed as a verification test in the present computations.

3. Numerical methodology

The size of the computational domain is $60\tilde{\Delta} \times 60\tilde{\Delta} \times 30\tilde{\Delta}$ along the streamwise, vertical and spanwise directions, respectively. Thus, the distance from the bottom boundary to the centreplane of the channel is 30 times the Stokes layer thickness. The selected domain size is exactly the same as that of Spalart & Baldwin (1989) and their domain is the largest and the most conservative among the different numerical studies. By examining the two-point correlation function, Ozdemir *et al.* (2010) showed that this domain size is sufficiently large to capture the main turbulent characteristics at $Re_\Delta = 1000$ in the case of a clear fluid.

The adequacy of spatial resolution is examined in terms of wall units. The friction velocity in dimensional terms is defined as

$$\tilde{U}_* = \sqrt{\frac{|\tilde{\tau}_w|}{\rho_f}}, \tag{3.1}$$

where $\tilde{\tau}_w$ is the wall shear stress. In non-dimensional terms, the friction velocity becomes

$$U_* = \sqrt{\frac{1}{Re_\Delta}\left|\left\langle \frac{\partial u}{\partial y} \right\rangle_w\right|}, \tag{3.2}$$

where $\langle \cdot \rangle_w$ represents an average over the bottom wall. The time history of the non-dimensional friction velocity and the corresponding centreline velocity is shown in figure 2 for the $Ri = 0, 1 \times 10^{-4}$ and 3×10^{-4} cases. Also shown in the figure is the definition of the phase (ϕ) adopted in this study. According to this definition, $\phi = 0$ corresponds to the phase of the maximum positive streamwise velocity, $\phi = \pi$ corresponds to the maximum negative velocity, and $\phi = \pi/2$ and $3\pi/2$ correspond to flow reversals. When $Ri = 0$ or 1×10^{-4}, the flow near the bottom wall remains turbulent and the friction velocity (correspondingly, wall shear stress) peaks at about the same time as the velocity maximum. For the case of $Ri = 3 \times 10^{-4}$, as discussed later, the flow near the bottom wall is laminarized and, as a result, the peak friction velocity leads the velocity maximum by $\pi/4$, in agreement with the expected behaviour of the laminar oscillatory Stokes layer.

The non-dimensional coordinate in wall units can be expressed as

$$\boldsymbol{x}^+ = U_{*,max} Re_\Delta \boldsymbol{x}, \tag{3.3}$$

where $u_{*,max}$ is the maximum non-dimensional friction velocity at the bottom wall. The results reported here were performed with a grid of $192 \times 193 \times 192$ points along the streamwise, wall-normal and spanwise directions. A uniform grid is used along the periodic streamwise and spanwise directions, but along the wall-normal direction, a non-uniform Chebyshev Gauss–Lobatto grid is used (Canuto *et al.* 1987). In the case of a clear fluid ($Ri = 0$), this grid yields a resolution of $\Delta x^+ = 15.6$ and $\Delta z^+ = 7.8$. Along the wall-normal direction, the resolution close to the wall is $\Delta y^+ = 0.2$, and at the channel centre the resolution is $\Delta y^+ = 24.5$. For the other three cases in which particles attenuate turbulence, the peak friction velocity is lower and as a result the grid resolution is even better.

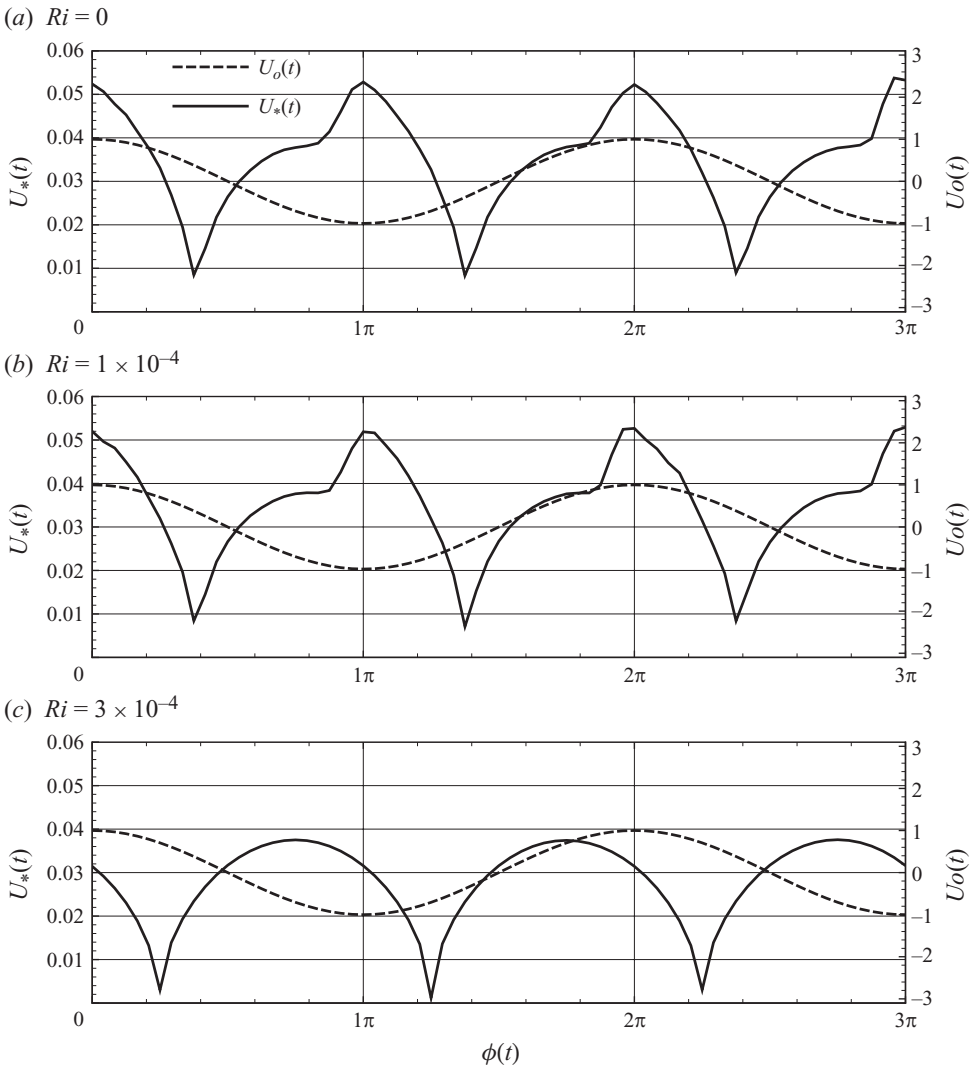

FIGURE 2. Time series of the friction velocity for (*a*) the passive, (*b*) $Ri = 1 \times 10^{-4}$ and (*b*) $Ri = 3 \times 10^{-4}$ cases. Also shown for reference (dashed lines) is the oscillatory far-field velocity at the centre of the channel.

The grid resolution used here is fine enough to capture the entire range of scales, which can be verified from the power spectrum of the velocity fluctuation. The adequacy of the present grid for the clear fluid has been established by Spalart & Baldwin (1989) and Ozdemir *et al.* (2010). Although we expect turbulence to weaken in the presence of suspended particles, here we confirm the adequacy of resolution for the $Ri = 1 \times 10^{-4}$ and 3×10^{-4} cases by plotting the corresponding velocity power spectra in figures 3 and 4. In figure 3, the streamwise and spanwise power spectra for $Ri = 1 \times 10^{-4}$ for all three components of fluctuating velocities at two different distances from the bottom wall ($y^+ = 1.8$ and $y^+ = 29$) are plotted at three different phases during the wave cycle. For reference, a $-5/3$ decay rate corresponding to the inertial range behaviour is shown by a thin straight line in the log–log plot. Owing to our choice of the modest Reynolds number and weak turbulence, an extended

https://doi.org/10.1017/S0022112010003769 Published online by Cambridge University Press

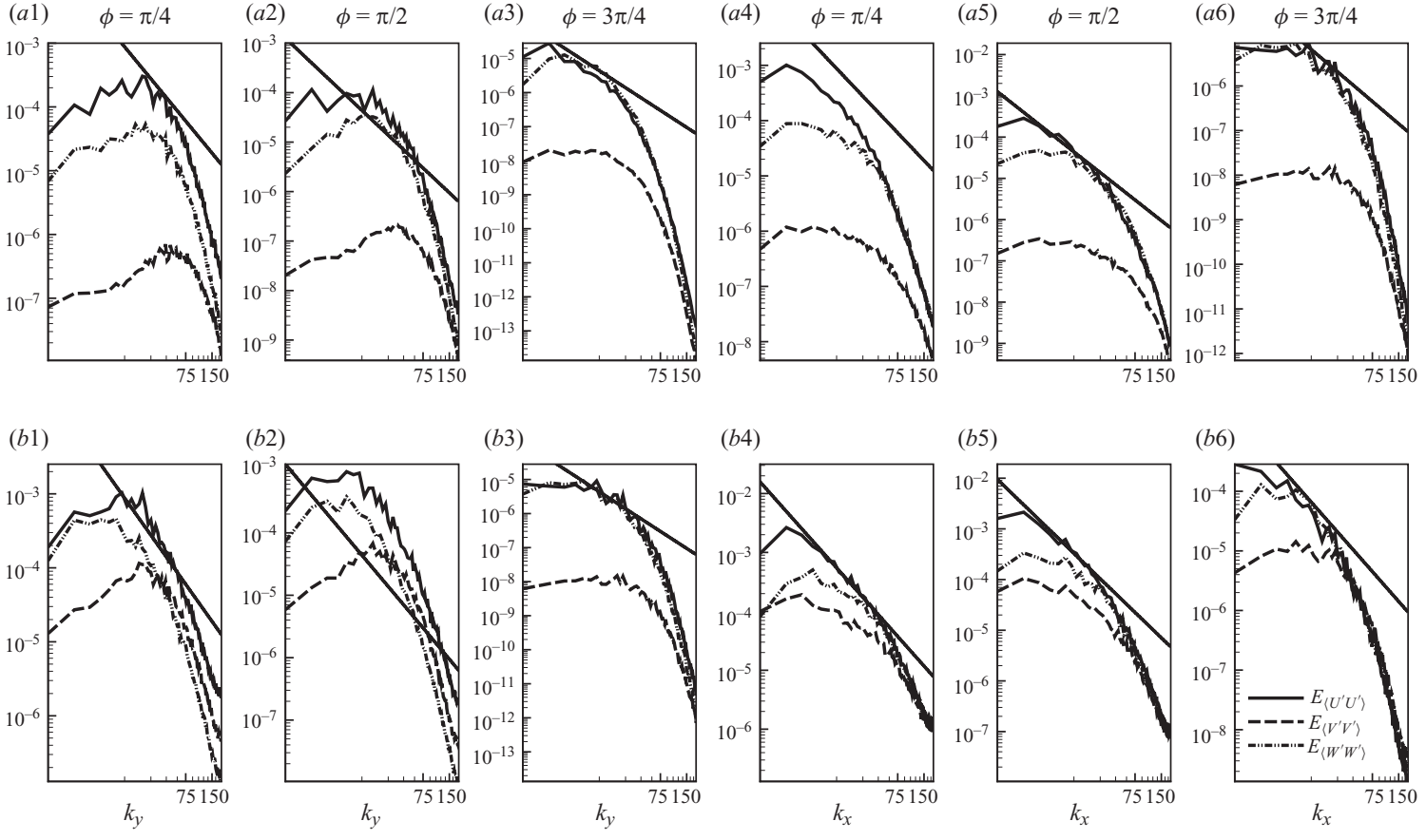

FIGURE 3. Power spectrum of velocity fluctuations for $Ri = 1 \times 10^{-4}$ measured at $y^+ = 1.8$ (row a) and $y^+ = 29$ (row b). Solid, dash-dotted and dashed lines show the power spectra of the streamwise, vertical and spanwise velocity fluctuations, i.e. $E_{\langle U'U'\rangle}$, $E_{\langle V'V'\rangle}$ and $E_{\langle W'W'\rangle}$. Columns 1–3 show the spanwise power spectrum and columns 3–6 show the streamwise power spectrum. In each case, results at three different phases are shown. The power spectra are obtained by averaging over the phase and horizontal planes.

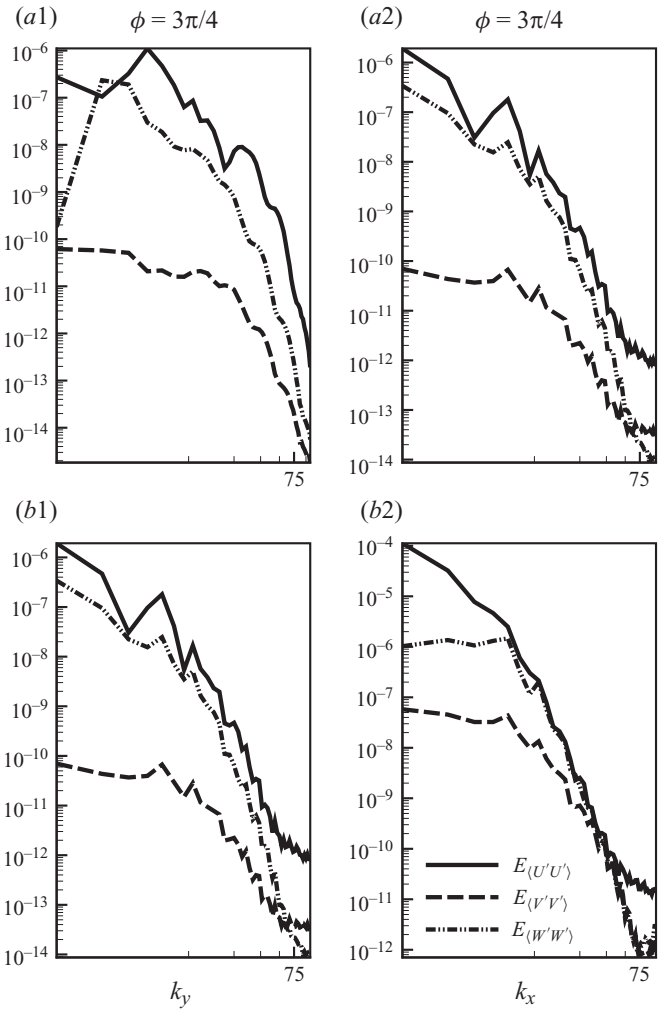

FIGURE 4. Power spectrum of velocity fluctuations for $Ri = 3 \times 10^{-4}$ measured at $y^+ = 1.8$ (row a) and $y^+ = 29$ (row b). Solid, dash-dotted and dashed lines show the power spectra of the streamwise, vertical and spanwise velocity fluctuations, i.e. $E_{\langle U'U'\rangle}$, $E_{\langle V'V'\rangle}$ and $E_{\langle W'W'\rangle}$. Results for only $\phi = 3\pi/4$ are shown. ($a1, b1$) The spanwise power spectrum and ($a2, b2$) the streamwise power spectrum.

inertial range is not observed. The fluctuating velocities are observed to decay by about 4 to 6 decades in the spanwise and streamwise spectra. The corresponding spectra for $Ri = 3 \times 10^{-4}$ are plotted only for $\phi = 3\pi/4$ (figure 4), and again several decades of decay can be observed in both the streamwise and spanwise spectra. As discussed later, at this Richardson number the flow near the bottom boundary laminarizes during part of the wave cycle and $\phi \approx 3\pi/4$ presents the highest demand for resolution. On the basis of the spectral decay, we conclude that the resolution employed in this study is sufficient for all the cases considered.

The flow field is time-advanced using the Crank–Nicolson scheme for the diffusion terms. The aliasing errors in the non-advective terms are removed with the Arakawa method and advanced with a third-order implicit Runge–Kutta scheme due to its low storage requirement. More details on the implementation of this numerical scheme

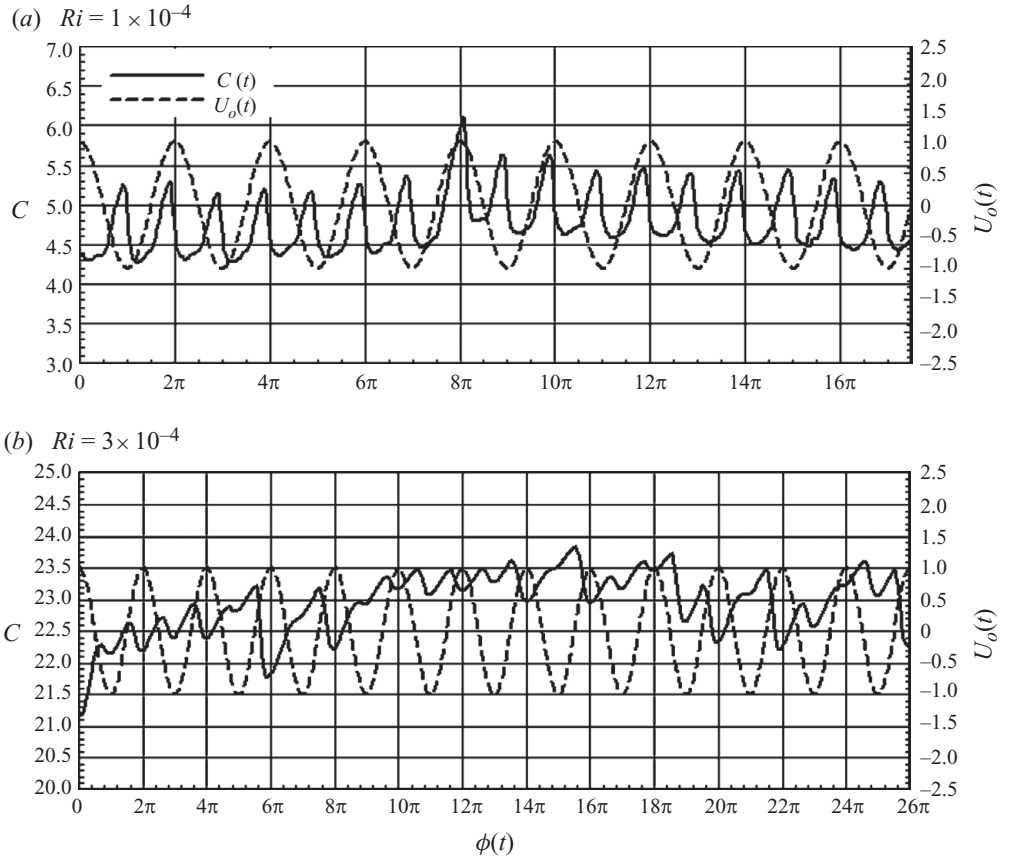

FIGURE 5. Time series of the plane-averaged particle concentration at $y^+ = 2$ for (*a*) $Ri = 1 \times 10^{-4}$ and (*b*) $Ri = 3 \times 10^{-4}$. Also shown for reference (dashed lines) is the oscillatory far-field velocity at the centre of the channel.

are given by Cortese & Balachandar (1995). The time step chosen for the simulations is 1/96 000 of the wave period, which maintains the Courant number to be below 0.5. Thus, each wave is resolved with almost 10^5 time steps. The simulation was typically evolved about six cycles or more in order for the initial transients to decay and the turbulence statistics to reach the stationary state. Figure 5 shows the time history of the planar-averaged concentration at an elevation very close to the bottom boundary ($y^+ = 0.2$) for the $Ri = 1 \times 10^{-4}$ and 3×10^{-4} cases. A perfectly periodic variation is not observed. Some cycle-to-cycle variation is observed, indicating sub-harmonic component of the disturbance. The time series of other turbulent statistics are similar in character. Figure 6 shows time evolution of the turbulent kinetic energy averaged over horizontal planes for the $Ri = 1 \times 10^{-4}$ (at $y^+ = 154$) and 3×10^{-4} (at $y^+ = 87$) cases. Here, again in the turbulent state, variations between cycles can be observed. Nevertheless, after a short transient a statistically stationary state can be observed. The time and phase-averaged statistics presented here were computed by averaging over the statistically stationary state. For example, for $Ri = 1 \times 10^{-4}$ last four cycles are used, whereas for $Ri = 3 \times 10^{-4}$ last nine cycles were used for averaging.

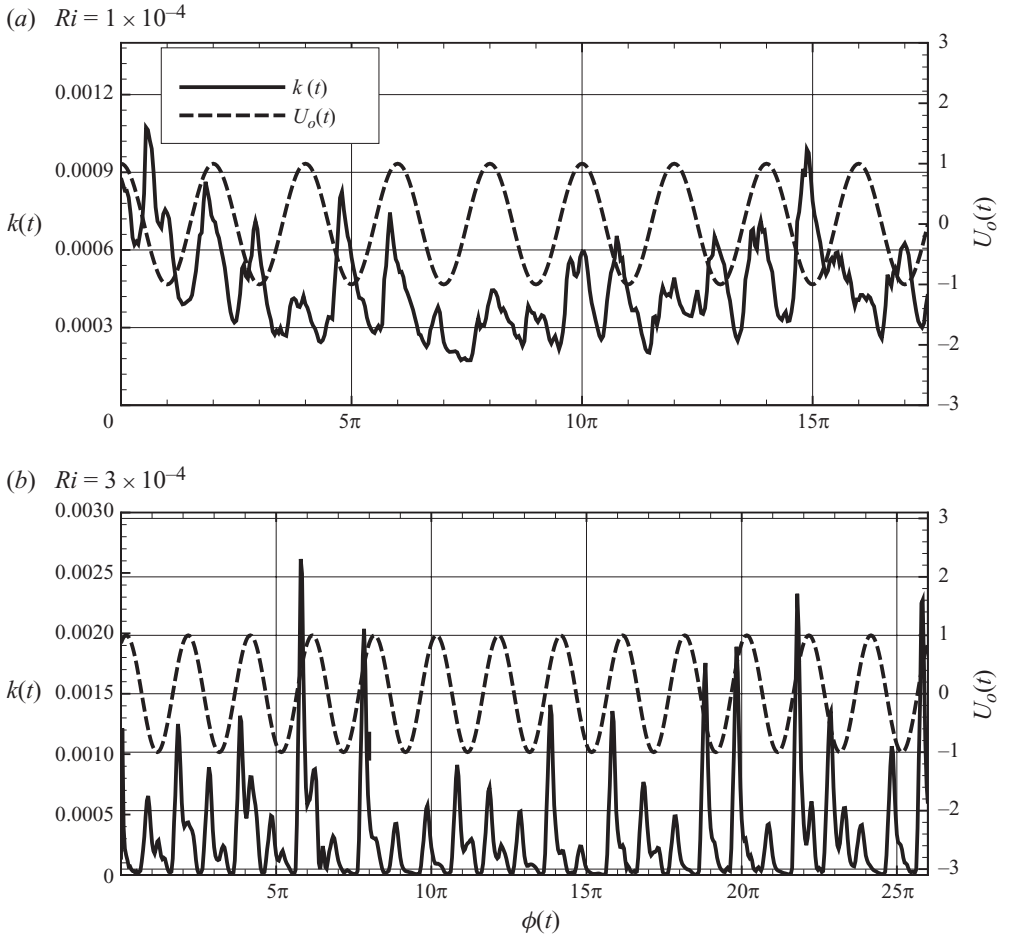

FIGURE 6. Time history of the turbulent kinetic energy for (*a*) $Ri = 1 \times 10^{-4}$ at $y^+ = 154$ and (*b*) $Ri = 3 \times 10^{-4}$ at $y^+ = 87$. Also shown for reference (dashed lines) is the oscillatory far-field velocity at the centre of the channel.

4. Results

In the literature of two-phase flow research, the turbulence modulation is affected by particle volume fraction, mass loading, response time of particles and settling velocity (see Balachandar & Eaton 2010 for a complete review), apart from parameters controlling the carrier phase. In the present simplified formulation, since the particle Stokes number is considered to be small, the two-phase flow can be collectively represented by four key parameters: the Reynolds number (Re_Δ), the bulk Richardson number (Ri), the non-dimensional settling velocity (V_s) and the Schmidt number (Sc). The turbulent nature of the flow is dictated by the Reynolds number with the intensity of turbulence increasing with increasing Re_Δ. The stabilizing effect on the flow turbulence is due to particle-induced density stratification. It can be deduced that turbulence modulation is effected by two parameters: Ri and settling velocity (V_s). Settling velocity determines the vertical variation of the particle concentration profile, while Ri can be thought of as a proxy for the volume-averaged particle concentration, which directly affects the carrier flow in the momentum equation. As a

Case	Re_Δ	Re_a	Ri	V_s	Sc
1	1000	500 000	0	9×10^{-4}	0.5
2	1000	500 000	1×10^{-4}	9×10^{-4}	0.5
3	1000	500 000	3×10^{-4}	9×10^{-4}	0.5
4	1000	500 000	6×10^{-4}	9×10^{-4}	0.5

TABLE 1. Simulations performed in this study. In all these simulations, the particle settling velocity, V_s, the Schmidt number, Sc, the Reynolds numbers Re_Δ and Re_a are kept constant, while the bulk Richardson number, Ri, is variable to identify the flow behaviour under different volume-averaged concentrations.

first step, in this study we focus on an oscillatory boundary layer of $Re_\Delta = 1000$, and the non-dimensional settling velocity is held constant at $V_s = 9 \times 10^{-4}$. Four different values of the bulk Richardson number are considered ($Ri = 0, 1 \times 10^{-4}, 3 \times 10^{-4}$ and 6×10^{-4}) in this study. The list of parameters employed in the simulations is given in table 1. As discussed below, the clear fluid ($Ri = 0$) is in the turbulent regime, while the fluid is fully laminarized at $Ri = 6 \times 10^{-4}$ and thus a range of behaviour is encountered.

4.1. *Laminar solution*

The role of the above-defined parameters can be explored in the laminar solution. The momentum equation (2.5) can be solved under the laminar flow condition, and in the limit of channel half-height being much larger than the Stokes layer thickness, the non-dimensional streamwise velocity in the bottom half of the channel is

$$U(y,t) = \sin\left(\frac{2t}{Re_\Delta}\right) + \mathrm{e}^{-y}\sin\left(y - \frac{2t}{Re_\Delta}\right). \tag{4.1}$$

The laminar solution shown above satisfies no-slip boundary condition at the bottom boundary ($y = 0$) and exponentially approaches the free-stream oscillatory flow. From the choice of the length scale, the non-dimensional thickness of the laminar boundary layer is unity. The laminar concentration profile is independent of the laminar velocity and is

$$C(y,t) = C_W \exp(-V_s Re_\Delta Sc\, y), \tag{4.2}$$

where the non-dimensional concentration at the wall is

$$C_W = (60 V_s Re_\Delta Sc)[1 - \exp(-60 V_s Re_\Delta Sc)]^{-1}. \tag{4.3}$$

For a sufficiently deep channel (i.e. $60 V_s Re_\Delta Sc \gg 1$), the wall concentration becomes $C_W \approx 60 V_s Re_\Delta Sc$. Note that the laminar concentration profile is independent of the bulk Richardson number and for the present choice of parameters, the wall concentration is 27 times the volume-averaged concentration. The laminar concentration also decays exponentially away from the bottom boundary and the concentration boundary layer thickness, $(V_s Re_\Delta Sc)^{-1}$, is 2.22 times the Stokes layer thickness. Note that in the laminar flow, sediment particles are suspended by shear-induced drag and lift forces in addition to the non-turbulent fluctuating motion of particles. The suspension process described is parameterized by a diffusion process (Fickian diffusion), where the diffusion coefficient is set proportional to the kinematic viscosity, ν_f. Note also that the volumetric concentration is $O(0.01)$, and it is safe to

assume that the change in the fluid viscosity due to suspension is minimal (∼1 %) and does not affect the laminar velocity profile.

From its definition shown in (2.9), the bulk Richardson number can be rewritten as

$$Ri = 18\frac{V_s}{Re_\Delta}\left(\frac{\tilde{\Delta}}{d}\right)^2 \bar{\tilde{C}}. \tag{4.4}$$

Thus, for a given oscillatory flow condition and particle properties (i.e. fixed settling velocity, Reynolds number and $\tilde{\Delta}/d$), the Richardson number becomes a measure of the volume-averaged particle concentration, $\bar{\tilde{C}}$, in the domain. It is of interest here to investigate the critical values of the particle concentration (or Ri) at which turbulent flow and particle transport dynamics become drastically distinctive. For example, we are interested in establishing the critical concentration where the effect of particle density stratification is negligibly small on the carrier flow. Also, it is of practical interest to evaluate the critical concentration (or Ri_{crit}) that causes flow laminarization and complete suppression of turbulence and mixing. The results presented here follow this objective. In § 4.2, the results are first qualitatively observed in terms of turbulent vortical flow structures and iso-surfaces of concentration. Mean flow quantities and turbulent intensities are presented in § 4.3 to examine the relationship between carrier mean flow, particle concentration and second-order turbulent statistics. The instability mechanisms are analysed in § 4.4 and the flux and gradient Richardson numbers are presented in § 4.5. In § 4.6, turbulence modulation is further analysed through the TKE budget equation.

4.2. *Turbulent structures*

Simulation results for the four different particle concentrations ($Ri = 0, 1 \times 10^{-4}$, $3 \times 10^{-4}, 6 \times 10^{-4}$) present rather different outcomes of the particle–turbulence interaction, which shall be qualitatively identified and described in terms of iso-surfaces of swirling strength (figure 7) and particle concentration (figure 8). Swirling strength (λ_{ci}) is the imaginary part of the complex eigenvalue pair of the local velocity gradient tensor. If all three eigenvalues of the velocity gradient tensor are real, then the local swirling strength is zero. The swirling strength is able to discriminate against regions of shear and extract only coherent vortex structures in turbulent flows (Zhou *et al.* 1999; Chakraborty, Balachandar & Adrian 2005). Turbulent structures shown here do not include the case of $Ri = 6 \times 10^{-4}$ as the turbulence is fully suppressed by the suspended particles. Hence, the flow is completely laminarized and there are no vortex structures.

The effect of increasing particle-induced density stratification is observed in figure 7, where the iso-surface of the constant swirling strength is shown at six different phases spanning half a wave cycle. For the case of $Ri = 0$ (see figure 7*a*), particles do not affect the carrier phase and thus turbulence corresponds to that of the clear fluid discussed by Spalart & Baldwin (1989). Let us first discuss the clear fluid limit. At $\phi = \pi/6$, the far field (in this case the mid-channel) is just past its peak forward velocity and a dense pack of near-wall vortical structures can be observed close to the bottom boundary. The vortex structures observed at $\phi = \pi$, when the far-field reverse flow reaches its peak, are qualitatively similar. Owing to temporal periodicity, vortex structures at $\phi = 0$ can be expected to be statistically similar to those observed at $\phi = \pi$, but with a reversed orientation along the streamwise direction, and thus are consistent with those observed at $\phi = 0$. As the free stream decelerates ($\phi = \pi/3$), the vortex structures thin out and move away from the bottom boundary. This process

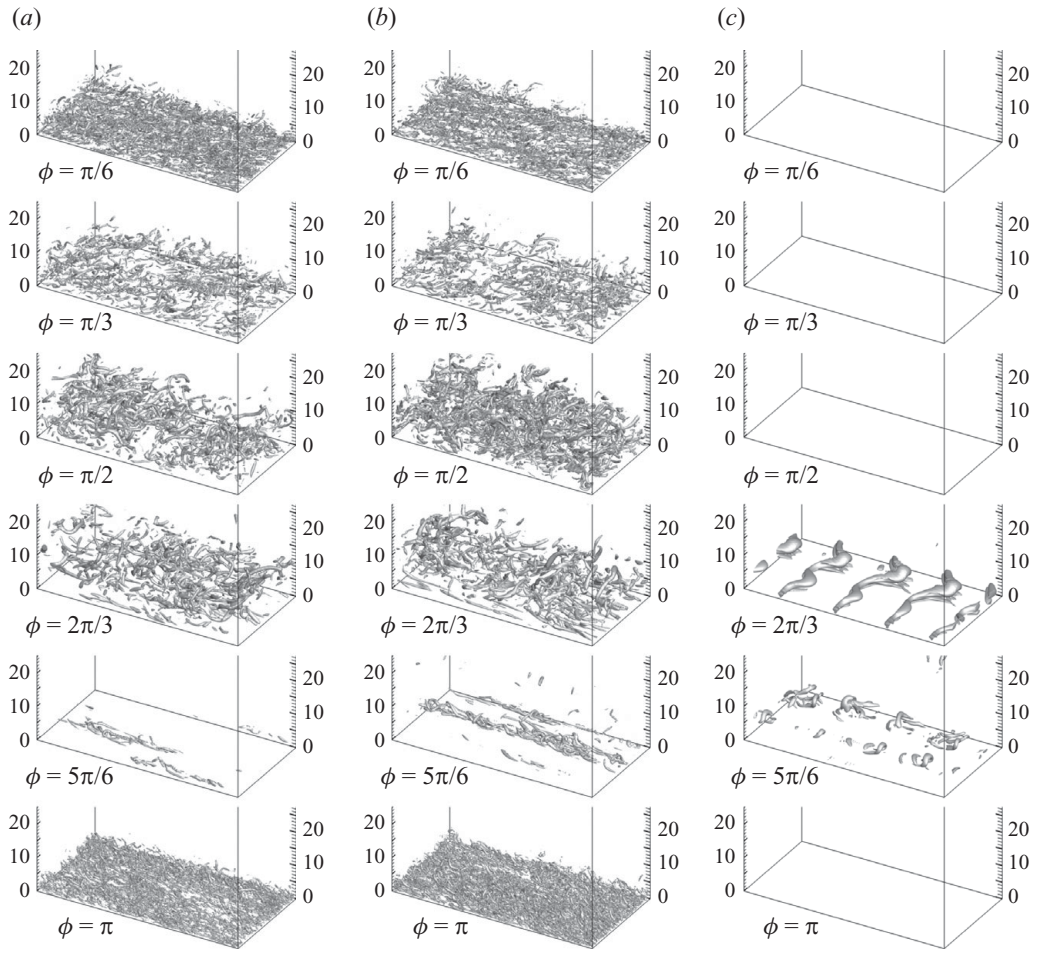

FIGURE 7. Turbulent vortical structures extracted in terms of iso-surfaces of the swirling strength (λ_{ci}). For a better view, $y = 0$ to $y \approx 25$ is focused, which is not indicated in the figure. The contour level chosen is $\lambda_{ci} = (0.1 \sim 0.2) \times \max(\lambda_{ci})$. Vortical structures are shown at six different phases, from $\phi = \pi/6$ to π for cases (*a*) $Ri = 0$, (*b*) $Ri = 1 \times 10^{-4}$ and (*c*) $Ri = 3 \times 10^{-4}$.

of outward migration continues during the flow reversal ($\phi = \pi/2$) and even past flow reversal ($\phi = 2\pi/3$). Clear signatures of typical shear layer turbulent structures, such as quasi-streamwise vortices and hairpin vortices, are observed. At $\phi = 5\pi/6$ when the reverse flow is accelerating in strength, only few streaky vortical structures can be observed. These streaky vortices are close to the bottom boundary and it appears that between $\phi = 2\pi/3$ and $\phi = 5\pi/6$ the turbulence observed away from the boundary at $\phi = 2\pi/3$ decays rapidly, and the near-wall structures observed at $\phi = 5\pi/6$ grow rapidly into fully developed turbulence when the reverse flow peaks at $\phi = \pi$. The observed behaviour is similar to that observed by Salon *et al.* (2007). The iso-contours of the concentration for the passive particle case ($Ri = 0$) shown in figure 8(*a*) depict a similar picture. Strong turbulent near-wall fluctuations can be seen during ($\phi = \pi$) and immediately following the peak velocity ($\phi = \pi/6$). The intensity of these fluctuations somewhat decreases during the deceleration phase, but persists even slightly after the flow reversal. The impact of the near-wall streaky vortical structures on the particle

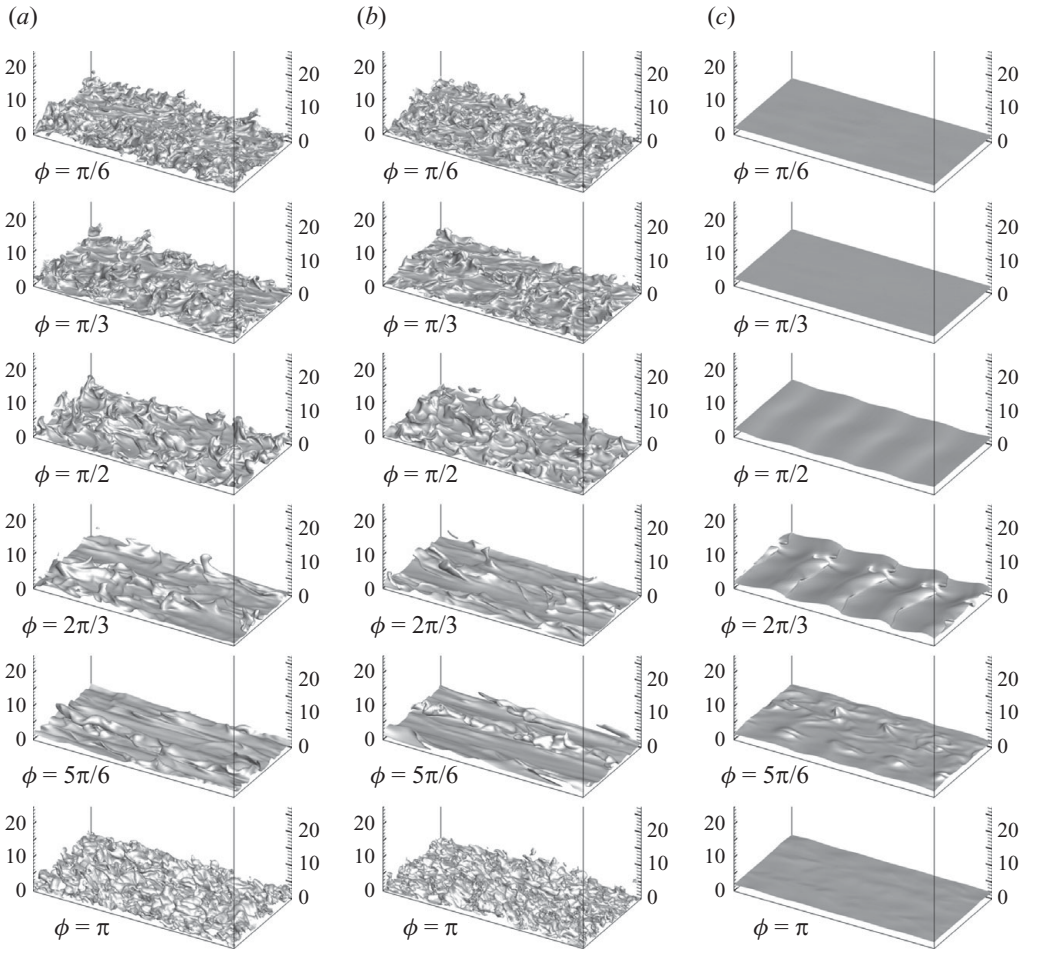

FIGURE 8. Turbulent vortical structures extracted in terms of iso-surfaces of particle concentration. For a better view, $y = 0$ to $y \approx 25$ is focused, which is not indicated in the figure. Concentration iso-contours are shown at six different phases, from $\phi = \pi/6$ to π for cases (*a*) $Ri = 0$, showing $C = 1.65$, (*b*) $Ri = 1 \times 10^{-4}$ showing $C = 2.0$ and (*c*) $Ri = 3 \times 10^{-4}$ showing $C = 10.0$.

concentration can be clearly observed at $\phi = 5\pi/6$. The turbulent bursts, which are the signature of an intermittent turbulent flow, can be clearly observed at phases $\phi = \pi/2$ to $\phi = 2\pi/3$.

The vortex structures for the case of $Ri = 1 \times 10^{-4}$ shown in figure 7(*b*) are statistically similar to those for the passive case. Similar observations can be made for the iso-surface of particle concentration (figure 8*b*), with the exception that the iso-surface level for $Ri = 1 \times 10^{-4}$ is chosen to be two times the volume-averaged concentration, which is slightly higher than that for the passive case. As discussed in detail when presenting the mean concentration profiles, increasing the Richardson number from 0 to 1×10^{-4} has a strong influence on the mean particle concentration. Since particle concentration in the bottom half of the channel increases substantially, a correspondingly higher contour level must be chosen to extract similar turbulent structures.

For the case of $Ri = 3 \times 10^{-4}$, vortex structures show a drastically different behaviour than that observed in the passive and $Ri = 1 \times 10^{-4}$ cases. First, there is no turbulent vortical structure observed in figure 7(*c*) at peak flow ($\phi = \pi$) and during the entire deceleration phase (see $\phi = \pi/6$ and $\phi = \pi/3$). This can be explained by turbulence suppression due to particle-induced stable density stratification. Although at flow reversal ($\phi = \pi/2$ in figure 7*c*) coherent vortex structures are not observed, the effect of incipient instability in terms of small-amplitude waves can be observed in the iso-surface of particle concentration in figure 8(*c*). These instabilities tend to grow from an earlier near-laminar condition ($\phi = \pi/6, \pi/3$) and reach peak amplitudes in the early acceleration phase around $\phi = 2\pi/3$. The instability appears as well-organized spanwise vortex rollers formed as a result of shear instability. The signature of the secondary instability can be seen as spanwise waviness of the vortex rollers (see $\phi = 2\pi/3$ in figure 8*c*). While relatively clean, small amplitude and nearly two-dimensional waves can be observed at $\phi = \pi/2$, a short time later at $\phi = 2\pi/3$ a more complex wave train with spanwise disturbances resembling wave-breaking formation is observed. At later stages of acceleration ($\phi = 5\pi/6$), both the vortex structure (figure 7*c*) and the iso-surface of concentration (figure 8*c*) show decay of the instabilities, and only a remnant of the vortex structure and its impact on particle concentration can be observed. Interestingly, at the end of the acceleration when the flow reaches the peak reverse flow ($\phi = \pi$), all disturbances seem to have decayed and the flow appears to be in a laminar state. Note that the concentration contour shown in figure 8(*c*) is 10 times the volume-averaged concentration, which is much higher than that of previous cases of lower *Ri*. As seen in § 3.3, for $Ri = 3 \times 10^{-4}$ the flow largely laminarizes and, as a result, the mean particle concentration close to the bottom wall significantly increases. In order to extract the effect of instability, which is located close to the bottom wall, it is necessary to choose a larger concentration value for the iso-surface of concentration field.

These instability features for the case of $Ri = 3 \times 10^{-4}$ observed in figures 7(*c*) and 8(*c*) resemble the shear instability noted by Strang & Fernando (2001). They investigate the behaviour of these interfacial shear instabilities with respect to changes in the bulk Richardson number. While for a small bulk Richardson number they observe pure Kelvin–Helmholtz (KH) billows, with the increase in *Ri* they observe a combination of KH billows plus Hőlmbőe waves. In the present problem, it is difficult to separate the exact characteristic of these structures and the associated instabilities as they occur in a transient manner over only a short duration near the flow reversal. This is unlike the case considered in Strang & Fernando (2001), where the instabilities occur in a quasi-steady manner and the effect of stratification can be considered almost constant.

4.3. *Mean quantities and turbulent intensity*

In this section, the interaction between the carrier flow and particles for $Ri = 0, 1 \times 10^{-4}$ and 3×10^{-4} is further analysed in terms of the statistically averaged particle concentration and velocity statistics. Statistics are obtained by averaging over horizontal planes and also over time instants of an identical phase. These averages are referred to as 'phase-average' and denoted by angle brackets. Note that the statistics during the forward flow ($-\pi/2 < \phi < \pi/2$) are related to statistics during the reversed flow ($\pi/2 < \phi < 3\pi/2$) as follows:

$$\langle C \rangle, U_{rms}, V_{rms}, W_{rms}(y, t = \phi) = \langle C \rangle, U_{rms}, V_{rms}, W_{rms}(y, t = \phi + \pi), \tag{4.5a}$$

$$\langle U \rangle, \langle UV \rangle, \langle UC \rangle, (y, t = \phi) = -\langle U \rangle, -\langle UV \rangle, -\langle UC \rangle (y, t = \phi + \pi). \tag{4.5b}$$

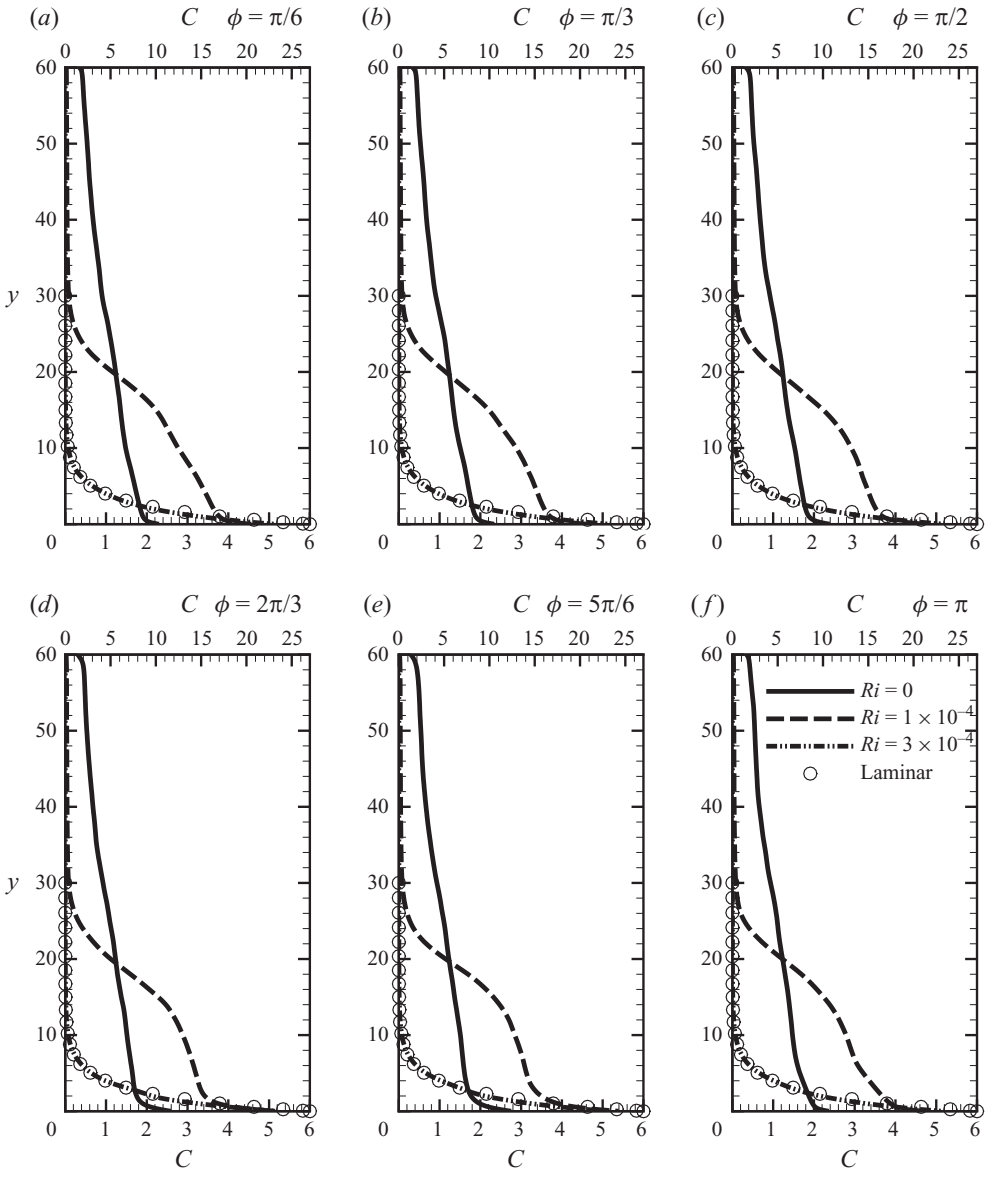

FIGURE 9. Mean concentration profiles for $Ri = 0$, 1×10^{-4} and 3×10^{-4} (refer to the upper axis for $Ri = 3 \times 10^{-4}$). (*a–f*) Six different phases during half a wave cycle are shown and the results for the other half of the wave cycle can be obtained from symmetry.

These symmetries are used to further enhance the statistics. Figures 9 and 10 show the averaged concentration and streamwise velocity profiles at six different distinct phases during the wave cycle for the $Ri = 0$, 1×10^{-4} and 3×10^{-4} cases. Note that the concentration scale for the $Ri = 3 \times 10^{-4}$ case is different from that of the other two cases in order to accommodate the rapid increase in the concentration towards the bottom wall. The averaged streamwise velocity profiles for $Ri = 0$ and 1×10^{-4} are almost identical (compare triangles and solid curves in figure 10). The corresponding root-mean-square (r.m.s.) turbulent velocities in the streamwise, wall-normal

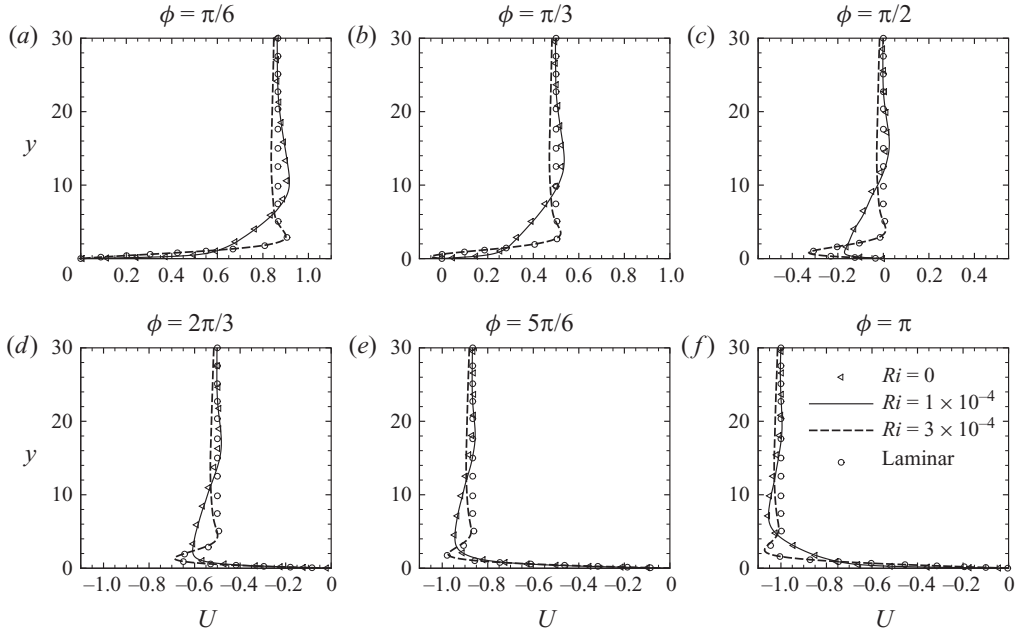

FIGURE 10. Mean streamwise velocity profiles for $Ri = 0$, 1×10^{-4} and 3×10^{-4}. (*a–f*) Six different phases during half a wave cycle are shown and the results for the other half of the wave cycle can be obtained from symmetry.

and spanwise directions at the six different phases are presented in figure 11. Again, it can be observed that the turbulent intensities for the $Ri = 0$ and 1×10^{-4} cases are of similar magnitude over much of the channel. In particular, there is little difference in turbulent intensities close to the bed between $y = 0$ and $y = 10$. However, closer to the mid-channel (from $y \approx 12$ to $y \approx 30$), although the overall magnitude of turbulent intensities becomes small, the turbulence intensity for $Ri = 1 \times 10^{-4}$ ranges only between 10 and 50 % of that for the $Ri = 0$ case.

The effect of reduced turbulence above $y \approx 15$ can be clearly seen in the mean concentration profiles shown in figure 9. For the passive case, the concentration profiles are more or less linear and particles are well-mixed over the entire channel, except for a thin layer of large concentration gradient very close to the bottom. On the other hand, for the $Ri = 1 \times 10^{-4}$ case, it can be observed that the particles are entrapped in the lower half of the domain and the concentration profile shows a clear feature of 'lutocline' (sharp negative concentration gradient). This shoulder-shaped concentration profile is predicted by Noh & Fernando (1991) for fine particles suspended in an oscillating grid flow due to the damping of turbulence kinetic energy by the particle-induced stable density stratification. It is also observed in the laboratory experiment with a similar oscillating grid set-up (Huppert *et al.* 1995). In the present simulation, the formation of lutocline can be clearly seen for fine-particle transport in the oscillatory boundary layer. Closer to the mid-channel, turbulence and mixing are suppressed due to the stabilizing effect of the large concentration gradient. Suppressed turbulence further prevents upward migration of particles, which would otherwise occur driven by turbulence. In this case, since the suppression of turbulence occurs near the mid-channel where the overall magnitude of turbulent kinetic energy

https://doi.org/10.1017/S0022112010003769 Published online by Cambridge University Press

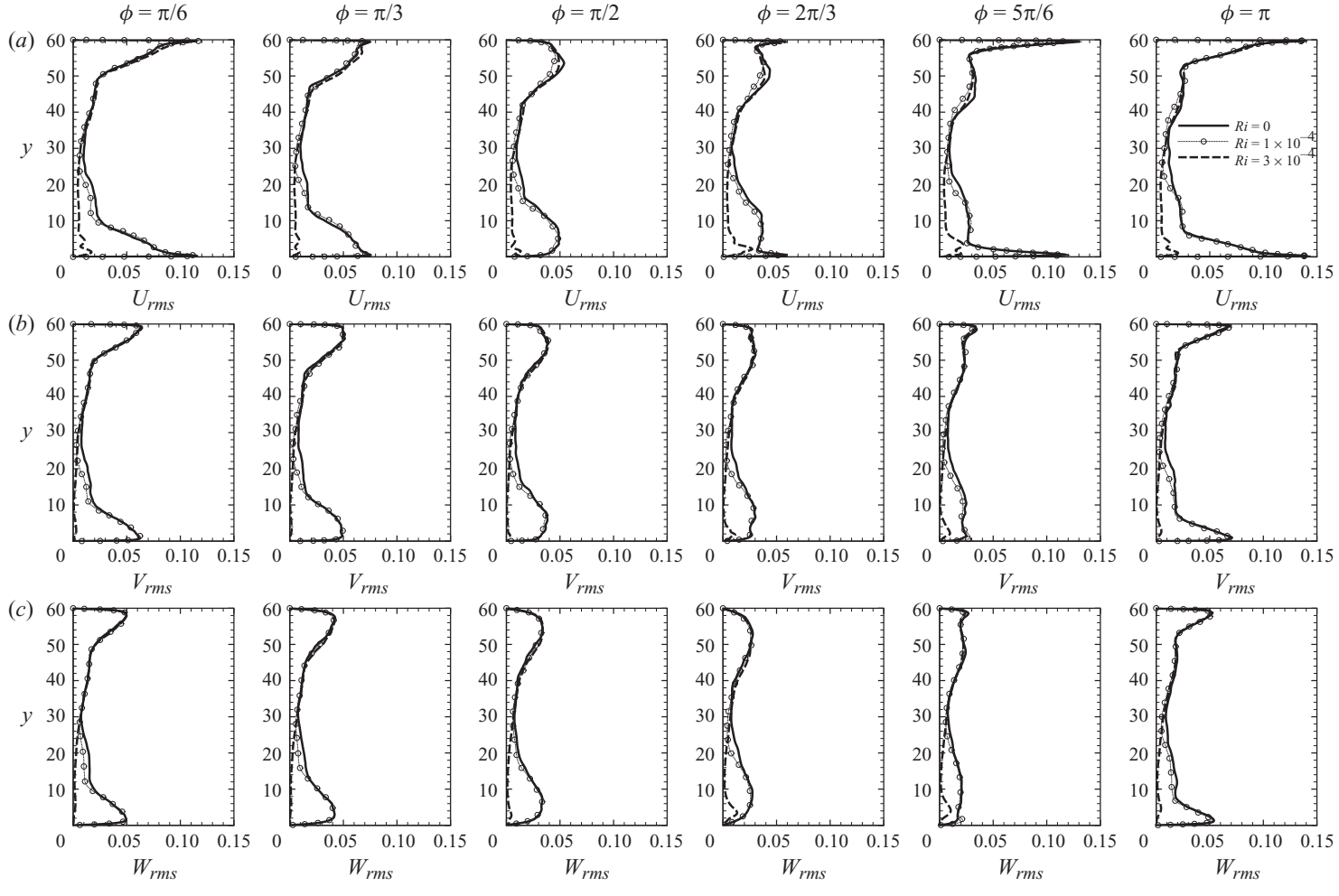

FIGURE 11. Turbulent r.m.s. velocity fluctuations along the (*a*) streamwise, (*b*) wall-normal and (*c*) spanwise directions. Six different phases during half a wave cycle are shown for $Ri = 0$, 1×10^{-4} and 3×10^{-4}.

is already small, turbulence modulation does not make a significant difference in the mean velocity profile. We shall discuss more field evidence of lutocline for the wave-driven fluid mud transport in § 4.

The characteristic of lutocline in an oscillatory boundary layer can be further investigated by closely examining the second quarter of the domain from the bottom boundary ($y = 15 \sim 30$). Figure 12 shows the iso-surface of concentration for the $Ri = 0$ and 1×10^{-4} cases at $C = 1.3$ for both cases to capture the turbulent structures in the region where turbulence is suppressed. A more quiescent behaviour can be observed for $Ri = 1 \times 10^{-4}$ compared with the passive case. Only larger wavelength undulations at a reduced amplitude can be seen for $Ri = 1 \times 10^{-4}$. Thus, as the Richardson number is increased from 0 to 1×10^{-4}, particle concentration is more noticeably affected than turbulent vortices. Examining the iso-surface of the swirling strength in the second quarter from the bottom wall (not shown here) also suggests that the turbulent structures below $y = 23$ are statistically similar for both $Ri = 0$ and 1×10^{-4}. Some reduction in vertical structures can be observed only closer to the mid-channel.

On the other hand, for the case of $Ri = 3 \times 10^{-4}$, we observe a significant difference in averaged mean velocity profiles (see figure 10) as compared to those for $Ri = 0$ or 1×10^{-4}. The velocity and particle concentration profiles in the bottom half of the channel are very close to the laminar profiles given in (4.1) and (4.2), which are also plotted in figures 9 and 10. The turbulent intensity in the wall-normal and spanwise components is nearly zero at time instants of velocity maximum (figure 11, $\phi = \pi$) and during the deceleration phase ($\phi = \pi/6$ and $\pi/3$). The r.m.s. streamwise fluctuation is also quite small close to the bottom boundary and appears to decay during the deceleration phase. However, starting from the flow reversal ($\phi = \pi/2$), the r.m.s. velocity components begin to grow during the acceleration phase in the region close to the bottom boundary ($0 \leqslant y \leqslant 9$). The fluctuation magnitudes appear to reach a peak around $\phi = 2\pi/3$ and then start to decay. During the entire period the r.m.s. velocity fluctuations for the case of $Ri = 3 \times 10^{-4}$ in the bottom half of the channel are substantially lower than those for the $Ri = 0$ and 1×10^{-4} cases. This reduction in turbulence is consistent with the vortical turbulent structures presented in figure 7.

The travelling wave character of the Stokes solution can be observed in both the laminar and turbulent streamwise velocity profiles. In figure 10, the variation of the averaged streamwise velocity along the vertical direction at all phases shows multiple local maxima and minima. From (4.1), it can be seen that for the laminar solution, a local minimum starts at the bottom boundary at $\phi = \pi/4$ and travels upward away from the bottom wall as the phase increases from $\pi/4$. The linear migration of the location of this minimum for the laminar solution is given by $y_{min,lam} = \phi + (\pi/4)$ and can be clearly followed during the acceleration phase from $\phi = \pi/2$ to $\phi = \pi$. In fact, in figure 10 the location of this minimum can be tracked further by switching to the lowest local velocity maximum at $\phi = \pi/6$ (owing to the left–right reflectional symmetry of the streamwise velocity profile). This qualitative behaviour of the Stokes solution can be observed in the turbulent velocity profile as well. Figure 13 shows the vertical location of the velocity extrema for both the turbulent ($Ri = 1 \times 10^{-4}$) and laminar cases ($Ri = 3 \times 10^{-4}$) as a function of the phase. In the turbulent case, a local minimum again forms at the bottom boundary slightly before $\phi = \pi/2$, but it travels away from the bottom boundary at a faster rate. In effect, at $Re_\Delta = 1000$ the turbulent Stokes boundary layer is about 4.5 times thicker than the corresponding laminar solution. The travelling wave character of the averaged solution is important,

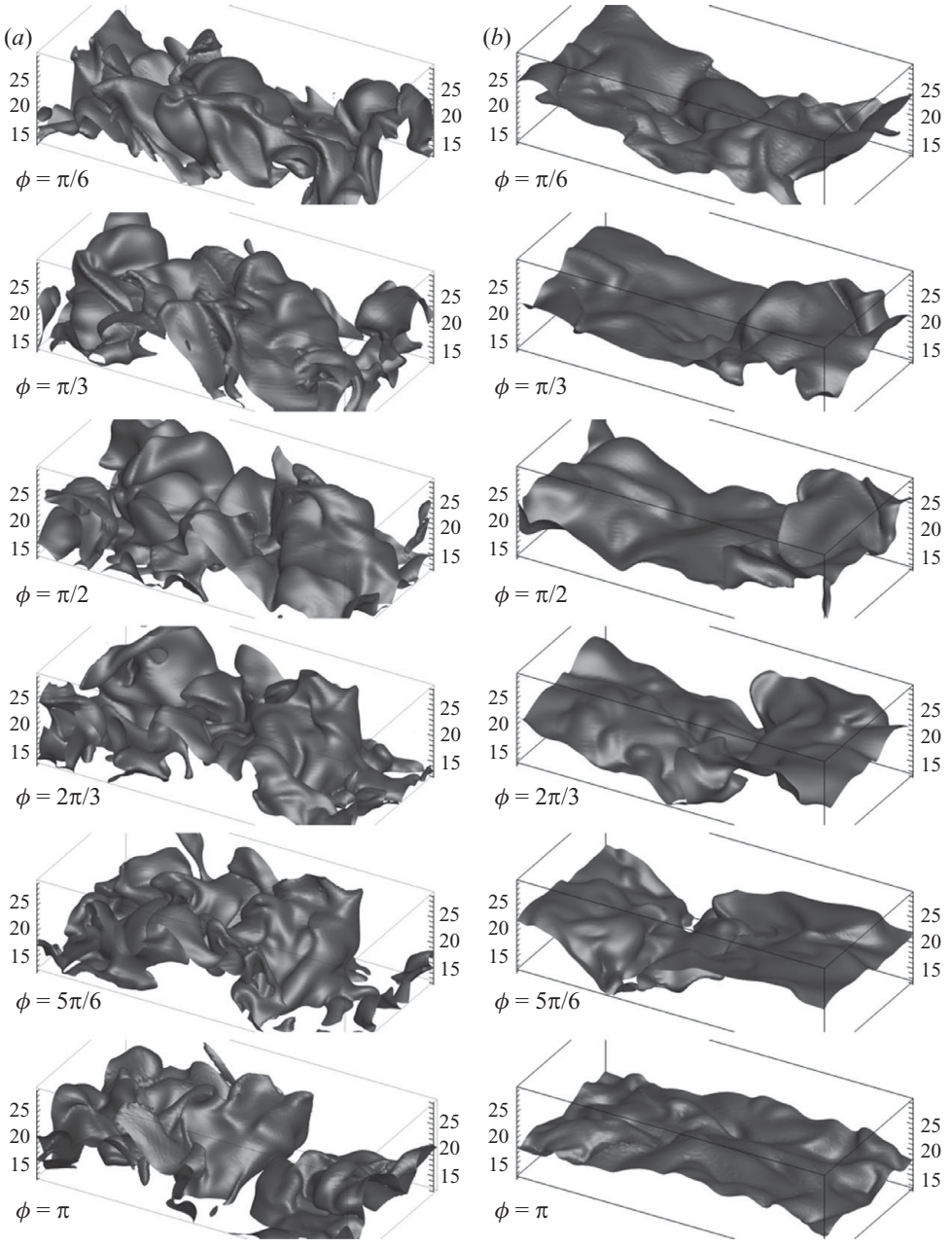

FIGURE 12. Iso-surfaces of the concentration at six different phases from $\pi/6$ to π for cases (*a*) $Ri = 0$ showing $C = 1.3$, (*b*) $Ri = 1 \times 10^{-4}$ showing $C = 1.3$. Note that only the middle third of the bottom half of the channel from $y = 15$ to $y = 30$ is shown.

since it implies inflection points in the velocity profile and can contribute to the onset of inviscid instability.

4.4. *Flow instability*

The clear appearance of coherent vortical structures in figure 7(*c*) and their temporal growth over part of the wave cycle, as implied in the iso-surface of concentration in

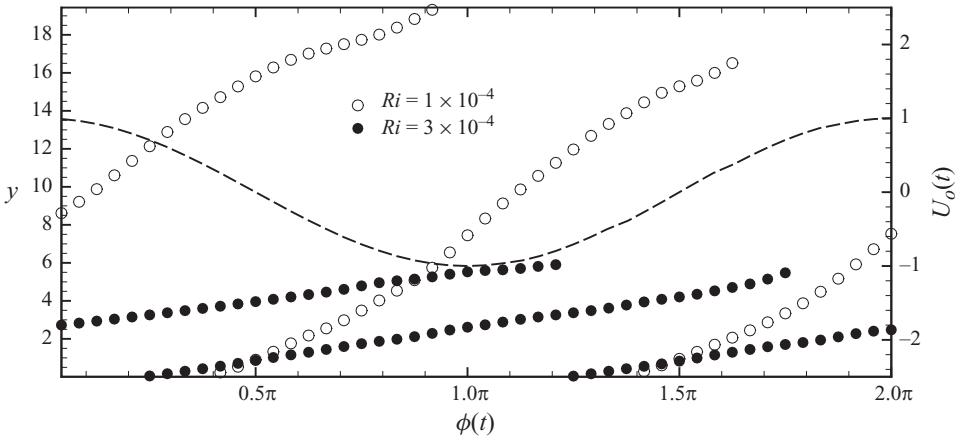

FIGURE 13. Time variation of extremum velocity for $Ri = 1 \times 10^{-4}$ and $Ri = 3 \times 10^{-4}$. Note that there exist phase slots where two extremum points are observed for both cases. Also shown for reference (dashed lines) is the oscillatory far-field velocity at the centre of the channel.

figure 8(*c*), raise interesting questions regarding this instability. A better understanding of this instability shall shed more light on the origins of fully developed turbulence in oscillatory boundary layers, with and without stratification. In this section, we are primarily concerned with the instability of the laminar profile.

4.4.1. *Stability of stokes layer*

The instability of the oscillatory Stokes layer and the transition to turbulence has not been fully understood even in the absence of particle concentration gradient induced stratification effects. A large discrepancy exists between experimental/computational observations and the results of the stability analysis (Blennerhassett & Bassom 2006). Initial attempts (Hall 1978) have not been fully successful in identifying unstable modes that could explain experimentally observed disturbances. A recent Floquet stability analysis of an oscillatory Stokes layer of semi-infinite extent by Blennerhassett & Bassom (2002) has yielded growing stationary and travelling mode disturbances with a critical Reynolds number of $Re_{\Delta,crit} \approx 1416$. They observed that the critical Reynolds number somewhat decreases with the presence of an upper boundary, but for the present half-channel height of 30 Stokes layer thickness, the effect on the critical Reynolds number is minimal. In contrast to the above theoretical result of the stability analysis, the present and prior simulations of the oscillatory Stokes layer show fully developed turbulence even at $Re_\Delta = 1000$ both in the decelerating and accelerating phases, close to $\phi = 0$ and $\phi = \pi$. As pointed out by Blennerhassett & Bassom (2006), this disagreement between theory and experiments/computations remains unexplained.

Nevertheless, here we will use results from the Floquet analysis of Blennerhassett & Bassom (2002) to better understand the unstable vortical structures observed for the case of $Ri = 3 \times 10^{-4}$. From their analysis, the critical streamwise wavelength can be estimated to be $16.77\tilde{\Delta}$. Although the growth rate of the Floquet disturbance has not been fully mapped out over the Reynolds number and wavenumber parametric space, the streamwise wavelength of the most unstable disturbance can be estimated to be similar at other Re_Δ. The four spanwise-oriented vortex rolls observed in figure 7(*c*), combined with the periodic streamwise extent of the computational domain, yield a wavelength of $15\tilde{\Delta}$. Of course, in the present simulation, since the streamwise

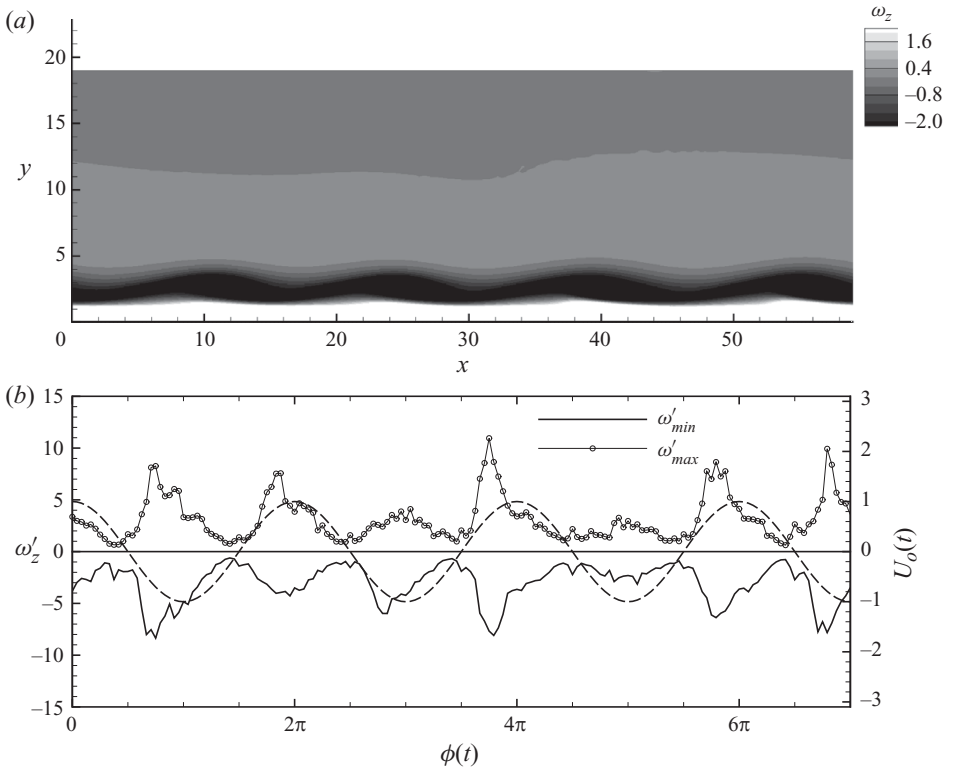

FIGURE 14. (*a*) Investigation of the onset of instability observed through contours of the span-averaged spanwise vorticity at ($\phi = 2\pi/3$). Dark regions indicate negative vorticity and roll-up of the negative vorticity into spanwise rollers can be observed. (*b*) The time history of the maximum and minimum vorticity observed in the aforementioned region. Also shown for reference (thin line) is the oscillatory far-field velocity at the centre of the channel.

length of the computational domain is chosen to be $60\tilde{\Delta}$, the possible disturbance wavelengths are limited to discrete choices.

An alternate view of the instability at $Ri = 3 \times 10^{-4}$ is presented in figure 14(*a*), where contours of the span-averaged spanwise perturbation vorticity are shown on the x–y plane at $\phi = 2\pi/3$. A periodic vortex roll-up can be observed and vortex structures are centred about $y \approx 3$. From figure 10, it can be observed that this location reasonably coincides with the inflection point of the mean velocity profile. The eigenfunction obtained by Blennerhassett & Bassom (2002) shows the disturbance to be located around $y \approx 5$ and occurs during the acceleration phase of the wave cycle. Shown in figure 14(*b*) are the time history of the peak perturbation spanwise vorticity (note both the positive and negative perturbations are plotted). A rapid increase in the perturbation vorticity during the flow reversal and the subsequent slow decay can be seen.

Despite the reasonable qualitative agreement we need to exercise caution in comparing the present simulation results with the Floquet stability analysis. First, the disturbances observed in figure 7(*c*) for $Ri = 3 \times 10^{-4}$ cannot be considered as unstable in the framework of the Floquet analysis. This disturbance only grew over part of the wave cycle, but decayed over the rest of the wave period. These disturbances were observed in the simulation at every cycle; however, as shown in figure 14(*b*), where the

peak spanwise vorticity was plotted as a function of time, the disturbance evolution was not strictly periodic. Second, although laminarization of the flow at $Ri = 3 \times 10^{-4}$ results in an oscillatory Stokes boundary layer and facilitates comparison with the Floquet stability analysis, the presence of the strong stable density stratification has not been accounted in the stability analysis of Blennerhassett & Bassom (2002). Clearly, the density gradient will contribute to the stability of the flow.

4.4.2. *Effect of density stratification*

The study on the effect of density stratification on the stability of shear layers dates back to the pioneering work of Taylor (1931). Miles (1961) and Howard (1961) established the condition that the gradient Richardson number, defined in terms of the present non-dimensional variables as

$$Ri_g = Ri \frac{\partial C}{\partial y} \Bigg/ \left(\frac{\partial U}{\partial y} \right)^2, \tag{4.6}$$

greater than 0.25 everywhere in the flow is the sufficient condition for stability. Thus, $Ri_g < 0.25$ somewhere in the flow would indicate instability. On the basis of the laminar velocity and concentration profiles given in (4.1) and (4.2), the gradient Richardson number as a function of distance from the bottom wall can be computed using the maximum value of the velocity gradient at that location during the wave cycle as (note that laminar concentration gradient is independent of time)

$$Ri_{g,laminar} = Ri\ H\ V_p^2\ Re^2 Sc^2 \exp[(2 - V_p\ Re\ Sc)y]. \tag{4.7}$$

In the present set of simulations, $V_s ReSc = 0.45$ and, as a result, the minimum value of the gradient Richardson number occurs at the bottom wall and is linearly dependent on the bulk Richardson number: $Ri_{g,laminar}(y \to 0) = 6.075 Ri$. Thus, for all values of Ri considered in this study, the gradient Richardson number at the wall is much smaller than 0.25. Since $Ri_{g,laminar}$ as defined above exponentially increases with y, only a layer close to the bottom boundary satisfies the condition $Ri_{g,laminar} \leqslant 0.25$. At $Ri = 1 \times 10^{-4}$ and 3×10^{-4}, the layer of the fluid given by $y \leqslant 3.88$ and $y \leqslant 3.18$ satisfies the condition for instability. The difference in the thickness of the unstable layer, as given by the gradient Richardson number, is only 20 %, but the resulting change in the character of the flow (see figure 7*b* versus figure 7*c*) is dramatic.

Of course, the condition $Ri_g < 0.25$ arises from an inviscid analysis and thus its relevance for the stability of a layer close to a solid boundary can be questioned. More importantly, the analysis of Miles (1961) and Howard (1961) is for a steady base flow and its applicability for the present oscillatory flow becomes relevant only if the time scale of the instability growth is much faster than the period of oscillation. It can be conjectured that at $Re_\Delta = 1000$ with a decreasing stratification effect (decreasing Ri) the growth rate of instability (seen in figure 7*c*) can increase dramatically to trigger the onset of turbulence quickly within part of the wave cycle. Thus, nonlinear effects can be expected to set in rapidly, and a Floquet analysis that assumes a linear behaviour for the disturbance over the entire wave cycle may not capture this fast transition to turbulence. Clearly, further investigation is needed on the instability mechanisms of an oscillatory boundary layer and the effect of stable stratification.

4.5. *Flux and gradient Richardson numbers*

Particle settling leads to density stratification, which attenuates boundary layer turbulence and the suppressed turbulence further encourages particle settling. According to such paradigm, it is believed that there exists a critical level of particle

concentration for a given turbulent flow such that major collapse of turbulence and particle settling may occur. Such behaviour in a steady flow has been well described by the flux and gradient Richardson numbers (e.g. Winterwerp 2001). Note that in this study, the forcing of the flow varies in time, which means that the competition between these mechanisms also varies over time. Therefore, the interrelation among particle settling flux, turbulent suspension flux and turbulence production is more complex. Nevertheless, we examine the role of particle-induced density stratification on the turbulence modulation through the gradient Richardson number, Ri_g, and the flux Richardson number, Ri_F. For the present case of the non-stationary turbulent flow, Ri_g and Ri_F are defined in terms of phase-averaged flow quantities as follows:

$$Ri_g = Ri \frac{\dfrac{\partial \langle C \rangle}{\partial y}}{\left(\dfrac{\partial \langle U \rangle}{\partial y}\right)^2}, \tag{4.8}$$

$$Ri_F = -Ri \frac{\langle C'V' \rangle}{\langle U'V' \rangle \frac{\partial U}{\partial y}}, \tag{4.9}$$

where primes indicate perturbation from the phase average. Both Ri_g and Ri_F are measures of turbulence attenuation due to stable density stratification versus turbulence production. Under the gradient diffusion assumption, the Reynolds stress and turbulent flux in the vertical direction can be written as follows:

$$\langle U'V' \rangle = -\nu_t \frac{\partial \langle U \rangle}{\partial y}, \langle C'V' \rangle = \frac{\nu_t}{Sc_t} \frac{\partial C}{\partial y}, \tag{4.10}$$

where ν_t is the turbulent viscosity and Sc_t is the turbulent Schmidt number, which is the ratio between the turbulent viscosity to turbulent diffusivity of particles. Hence, it can be shown that these two Richardson numbers are qualitatively equivalent. Although the gradient Richardson number, Ri_g, relies on the validity of the gradient diffusion assumption, it is a commonly used parameter in the stratified flow literature because it is easier to measure in laboratory and field experiments. In addition, in the literature of stratified flows for the thermal field, it has been observed that at a moderately stratified condition the gradient diffusion assumption holds true and the turbulent Prandtl number, Pr_t, is more or less constant. Pr_t plays the role of Sc_t in thermally stratified flows (Ivey & Imberger 1991; Schumann & Gerz 1995; Armenio & Sarkar 2002). We shall examine this issue in more detail for fine particle-laden flows below.

Both Ri_g and Ri_F are presented for the $Ri = 1 \times 10^{-4}$ and $Ri = 3 \times 10^{-4}$ cases at six different phases during the wave cycle (see figure 15). For the case of $Ri = 1 \times 10^{-4}$ (figure 15*a*), there are sharp jumps observed both in Ri_g and Ri_F due to velocity peaks near the top of the oscillatory boundary layer which make both Ri_g and Ri_F show a singular-like behaviour. The velocity peaks can be clearly observed in figures 10 and 13. Nevertheless, our interpretations are based on the overall trend of Ri_g and Ri_F. The magnitudes of Ri_g and Ri_F are generally small below $y = 12 \sim 18$ (the thin vertical line represents the critical value of 0.25 to be used as a reference). The small values of the Richardson numbers suggest that in the lower portion ($y < 12 \sim 18$) of the particle-laden oscillatory boundary layer, the flow remains turbulent. The domination of turbulence is in accordance with the turbulent intensities discussed in § 3.3. On the other hand, between $y = 12$ and $y = 18$, both Ri_g and Ri_F increase

https://doi.org/10.1017/S0022112010003769 Published online by Cambridge University Press

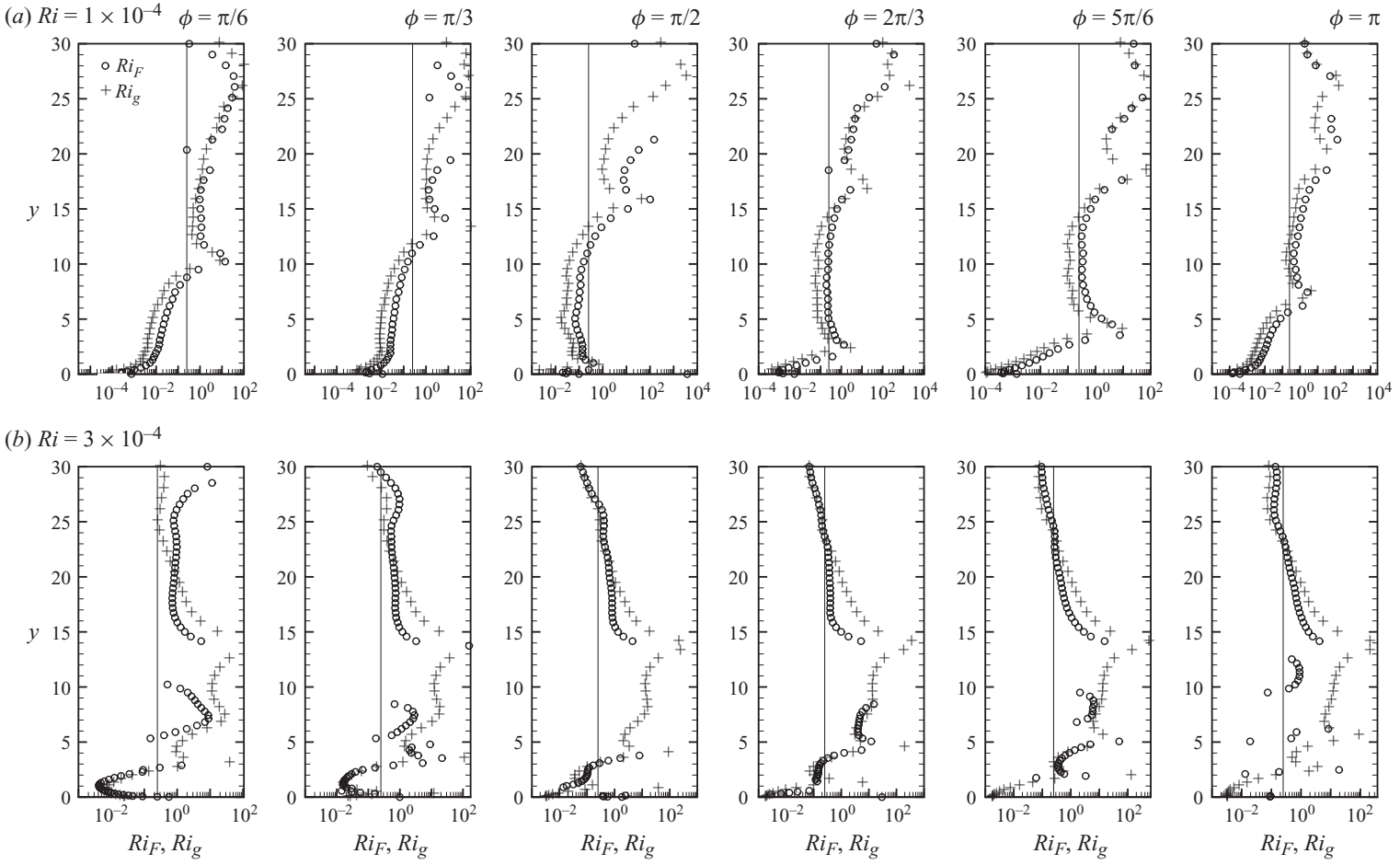

FIGURE 15. Plot of the flux and gradient Richardson number at six different phases for (*a*) $Ri = 1 \times 10^{-4}$ and (*b*) $Ri = 3 \times 10^{-4}$ in the log scale.

considerably, suggesting damping of turbulence due to stable density stratification. This regime also coincides more or less with the location of lutocline where a large negative particle concentration gradient exists (see figure 9).

Between $y = 15$ and 24, Ri_F sometimes takes values that cannot be plotted on a log–log scale, which can be seen as gaps in the plots at these elevations (see figure 15*b*). Such out-of-range values of Ri_F obtained here are due to negative (or near zero) particle suspension flux $\langle C'V' \rangle$. The ratio of particle suspension flux to the settling flux is shown in figure 16(*a*). This ratio, by definition, is identically zero at the bottom wall. It quickly increases away from the wall and roughly reaches a constant $O(1)$ in the lower portion of the boundary layer during the deceleration phase ($\phi = \pi,\ \pi/6,\ \pi/3$). At $\phi = \pi$ this layer is somewhat narrow and extends from the wall to only about $y < 4.5$. During the deceleration and flow reversal ($\phi = \pi/6,\ \phi = \pi/3$ and $\phi = \pi/2$), the thickness of this layer, where the particle–turbulent concentration flux nearly counterbalances the settling flux, increases and extends to about $y < 18$. Immediately following the flow reversal, turbulent flux decreases in the acceleration phase. Once again, only at the end of the acceleration phase ($\phi = \pi$) does the turbulent flux within the layer close to the wall substantially increase. This cyclical waxing and waning of turbulent flux is consistent with the intensity of turbulent structures shown in figure 7.

The behaviour for $y > 18$ is different. During substantial portion of the wave cycle, the turbulent particle flux is quite small and in fact $\langle C'V' \rangle$ at times becomes negative. In this region, the turbulence effect is considerably weaker and particle motion is dictated by the instantaneous local downward advective motion, especially immediately after the flow reversal. As a result, the net plane-averaged concentration flux in the vertical direction is negative. Clearly, such a downward advection cannot be described by the gradient diffusion assumption. The above observation implies that the turbulence production is significant only over the region $0 < y < 18$. Note that from the averaged streamwise velocity profile (figure 10), it can be seen that for $Ri = 1 \times 10^{-4}$, $y \approx 18$ is the approximate upper edge of the oscillatory boundary layer, above which the velocity remains nearly a constant. In the literature on highly stratified steady flows, negative Ri_F is observed with the increase in Ri_g (Ivey & Imberger 1991; Schuman & Gerz 1995; Armenio & Sarkar 2002). This behaviour can also be observed in Sc_t (see figure 17*a*). Starting from the bottom at $y = 20$, Sc_t remains constant, apart from the jumps due to very small velocity gradient. This also suggests an increase in Ri_F from $O(0.01)$ to $O(1)$ with respect to Ri_g. From $y = 20$ until the mid-channel, Ri_g increases to $O(100)$ and a negative flux is observed for phases $\phi = \pi/6$, $\pi/3$ and $\pi/2$, which can be seen as negative Sc_t values. For the phase $\phi = 5\pi/6$, Sc_t is observed to be highly fluctuating above $y = 20$. From these results we can clearly observe that the gradient diffusion assumptions hold true from $y = 0$ to $y = 20$. The deviation starting from $y = 20$ stems from the small values of the velocity gradient.

For the case of $Ri = 3 \times 10^{-4}$, it can be seen that the regime of small Ri_g and Ri_F exists only very close to the bed ($y = 0 \sim 3$). The sharp increases in the Richardson numbers for $Ri = 3 \times 10^{-4}$ are due to local averaged velocity gradients becoming zero rapidly away from the bed. The velocity gradients become zero where the averaged streamwise velocity reaches maximum and minimum values. As discussed in § 3.3, the initiation of a velocity minimum at the wall around $\phi = \pi/4$ and its migration away from the bottom wall with time can be clearly followed in figure 15(*b*) in terms of the location of the sharp peaks. As seen in the averaged streamwise velocity profiles, such maxima and minima are also observed for $Ri = 1 \times 10^{-4}$; however, owing to a

https://doi.org/10.1017/S0022112010003769 Published online by Cambridge University Press

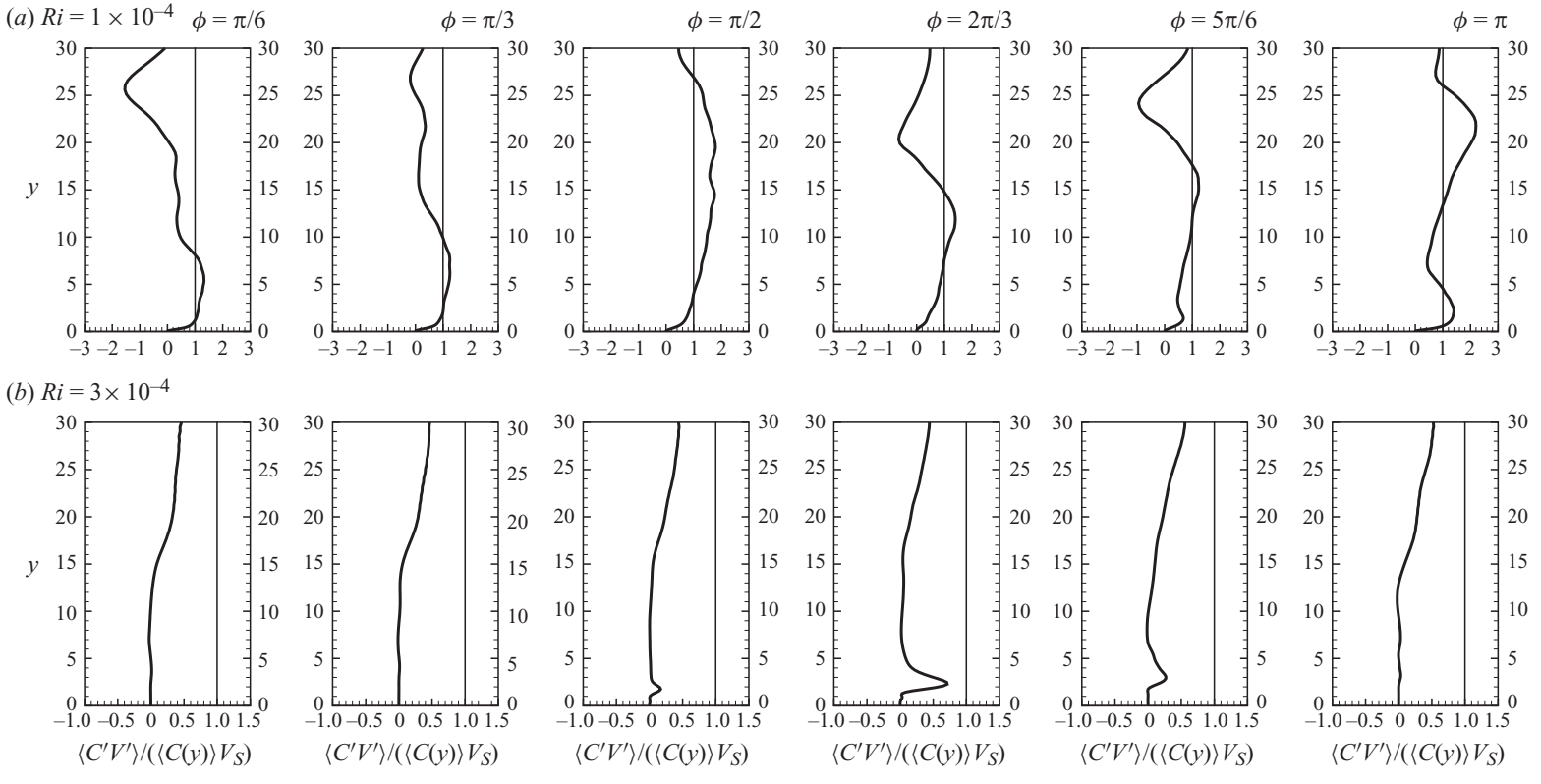

FIGURE 16. The ratio of the turbulent particle suspension flux over the settling flux for (*a*) $Ri = 1 \times 10^{-4}$ and (*b*) $Ri = 3 \times 10^{-4}$.

https://doi.org/10.1017/S0022112010003769 Published online by Cambridge University Press

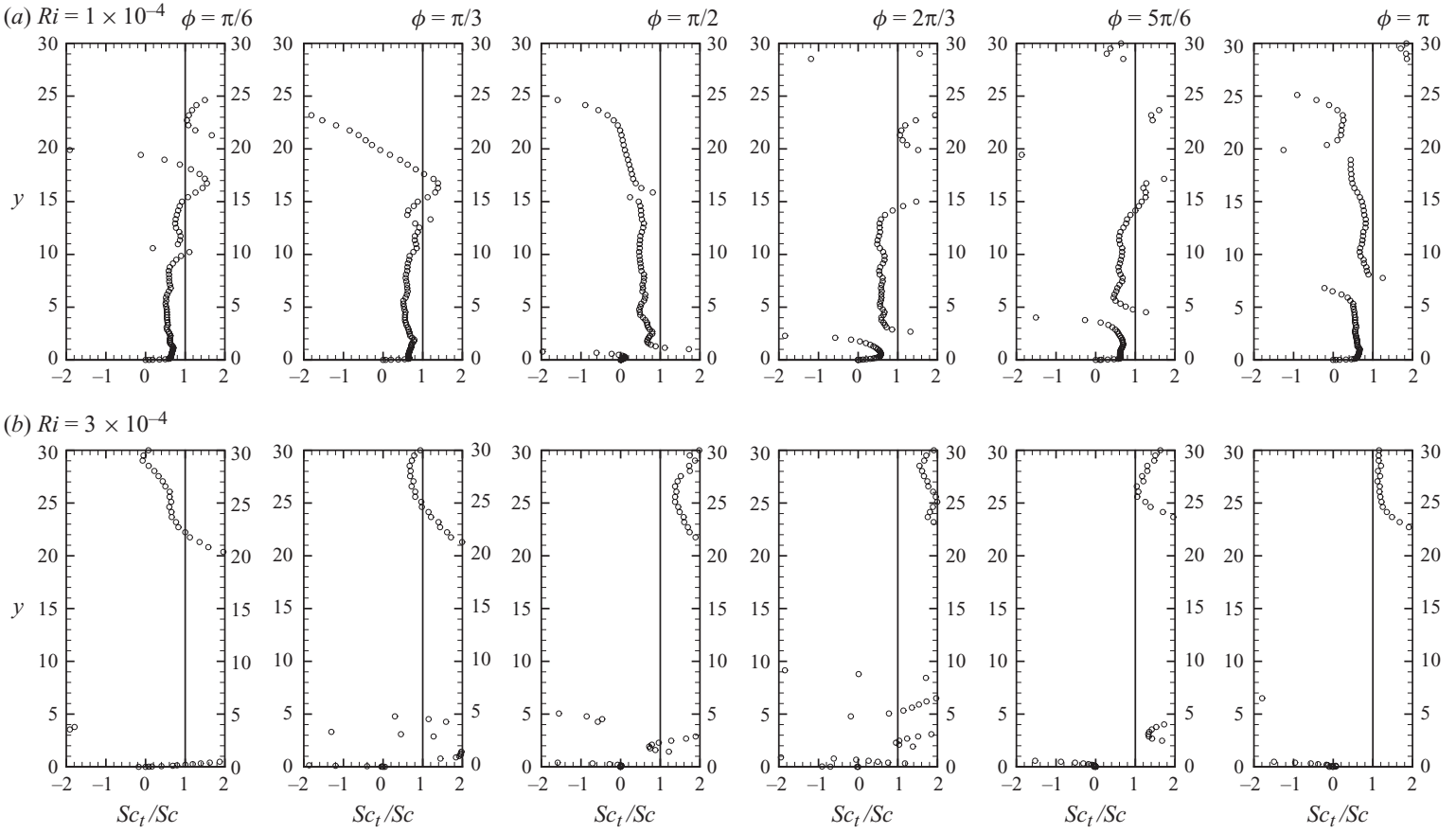

FIGURE 17. Variation of Sc_t/Sc between $y = 0 \sim 30$ at six different phases for (*a*) $Ri = 1 \times 10^{-4}$ and (*b*) $Ri = 3 \times 10^{-4}$. The perpendicular line is $Sc_t/Sc = 1$ and shown as a reference. For $Ri = 1 \times 10^{-4}$, shown in row (*a*) starting from a point at $0 < y < 1$ to $y \approx 20$, the value of Sc_t/Sc varies between 0.7 and 0.9, which shows a linear correlation between Ri_g and Ri_F. For $Ri = 3 \times 10^{-4}$, shown in row (*b*) Sc_t/Sc shows very random behaviour again due to velocity gradient.

stronger turbulent mixing near the bed, the regime of sharp increase of Ri_g is located farther away from the bed.

Above $y \approx 3$, both Ri_g and Ri_F maintain their large magnitudes (Ri_g and $Ri_F \gg 0.25$) for the case of $Ri = 3 \times 10^{-4}$. Again, this is consistent with the location of a large negative concentration gradient observed near the bed (see figure 9). In figure 7(*c*), we have observed shear instability generated during the flow reversal ($\phi = \pi/2$), which intensifies at early acceleration ($\phi = 3\pi/2$) with a subsequent decay till peak velocity ($\phi = 5\pi/6,\ \pi$). This interesting time-dependent feature cannot be observed in the gradient Richardson number profiles as they are qualitatively dictated by the laminar profiles at all phases. This is because the fluctuation level is not strong enough to create major change in the statistically averaged quantities. On the other hand, the flux Richardson number profiles show a slightly better picture of the instantaneous mixing process. Velocity fluctuations appear to have a greater effect as shear instability intermittently enhances perturbations during the flow reversal. However, the overall level of velocity fluctuation is relatively low in this case. The laminar boundary-layer thickness is very small compared with its turbulent counterpart and the velocity reaches a constant value over most of the domain. Therefore, both Ri_g and Ri_F, which are dependent on the mean velocity profiles, take large values. This further translates to large seemingly random fluctuations in Sc_t (see figure 17*b*). Therefore, both Ri_g and Ri_F are not very effective parameters to identify shear instability. On the other hand, we observe that the ratio of particle suspension flux to settling flux provides better information to identify shear instability during the flow reversal (see figure 16*b*). The suspension flux is very small across the channel over much of the wave cycle when compared with the settling flux. At flow reversal and during the acceleration phase, the suspension flux becomes large near the bed and in fact at $\phi = 2\pi/3$ the ratio of particle suspension flux to settling flux reaches 0.75 at $y \approx 2.5$. The vertical location of this increased suspension flux corresponds well with the location of the vortex structures seen in figure 14.

4.6. *TKE budget*

Simulation results presented so far identify several critical phenomena, such as the formation of lutocline and occurrence of instability during the flow reversal, as Ri (i.e. particle concentration) increases. It is clear that these phenomena are due to different degrees of particle–turbulence interaction in the oscillatory boundary layer. In this section, we demonstrate that the mechanisms causing these critical phenomena can be explained via the budget of the TKE, denoted as k in this study. The TKE budget equation for the present problem can be written as

$$\frac{\partial k}{\partial t} = -\frac{\partial \langle u_i \rangle}{\partial x_j} \langle u_i' u_j' \rangle - \frac{1}{Re_\Delta} \left\langle \frac{\partial u_i'}{\partial x_j} \frac{\partial u_i'}{\partial x_j} \right\rangle - Ri \langle C' u_i' \rangle \delta_{i2} - \left\langle \frac{\partial P'}{\partial x_i} u_i' \right\rangle - \frac{\partial}{\partial x_j} \left\langle \frac{1}{2} u_i' u_i' u_j' \right\rangle + \frac{1}{Re_\Delta} \frac{\partial^2}{\partial x_j^2} \left\langle \frac{1}{2} u_i' u_i' \right\rangle. \quad (4.11)$$

The term on the left-hand side is the time derivative of the TKE. The six terms on the right-hand side are the turbulent production, turbulent dissipation, particle-induced buoyancy dissipation/production, pressure transport, turbulent advection and viscous diffusion, respectively. For convenience, pressure transport, turbulent advection, and viscous diffusion (the last three terms on the right-hand side of (4.11)) are collectively presented as total transport in the TKE budget presentation (see figures 18–21).

https://doi.org/10.1017/S0022112010003769 Published online by Cambridge University Press

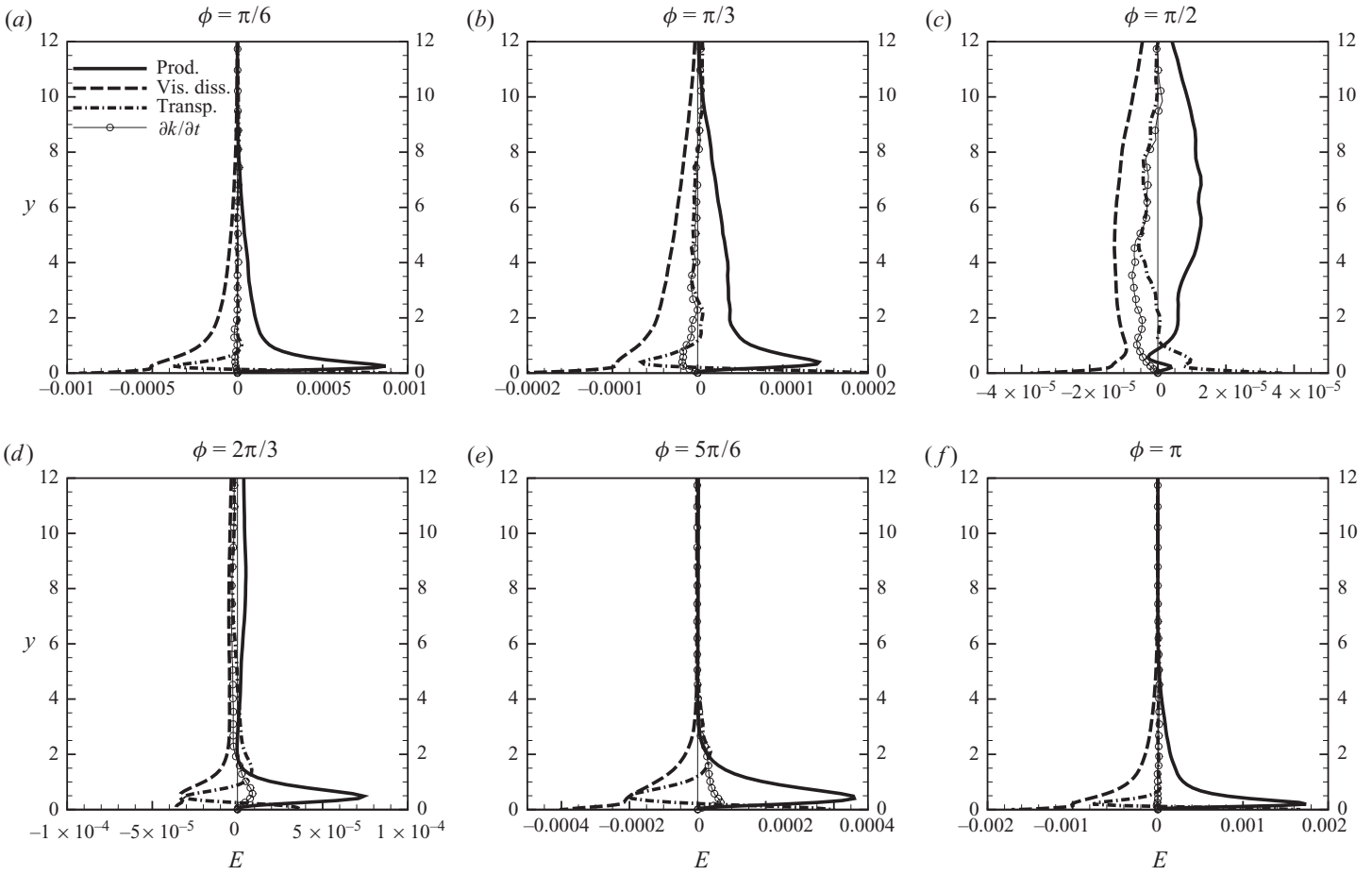

FIGURE 18. (*a–f*) Profiles of the TKE budget terms for $Ri = 0$ at $y = 0 \sim 12$. Plotted are the turbulent production (Prod.), viscous dissipation (Vis. diss.), total kinetic energy transport (Total transp.), which is the sum of the diffusion, turbulent advection and pressure transport terms, and the time rate of change in the TKE ($\partial k/\partial t$).

For the case of $Ri = 0$, where particles are passive to the carrier flow, the leading contributions are from turbulent production and turbulent dissipation within the oscillatory boundary layer (see figure 18 for $y = 0 \sim 12$). Production and dissipation are more or less in balance with each other except within $y < 1$ (corresponds to within 50 wall units), where total transport becomes comparable especially during and after the flow reversal ($\phi = \pi/2,\ 2\pi/3,\ 5\pi/6$). The time rate of change in the TKE (i.e. $\partial k/\partial t$) is relatively unimportant within the oscillatory boundary layer. The temporal flow characteristics of the oscillatory flow can be observed from turbulence production which correlates with the mean velocity gradient. From the flow reversal ($\phi = \pi/2$) to during the accelerating phase ($\phi = 2\pi/3,\ 5\pi/6,\ \pi$), the production term increases significantly (by three order of magnitudes) close to the bottom wall and fades away moving away from the wall. On the other hand, during deceleration ($\phi = \pi/6,\ \pi/3,\ \pi/2$), turbulent production near the bed almost decays completely (Hino *et al.* 1983). Near the top and above the oscillatory boundary layer (see figure 19*a* for $y = 15 \sim 25$), a very different TKE budget balance can be observed. First, the intensities of these terms are two to three orders of magnitudes smaller than those within the oscillatory boundary layer. Moreover, turbulent production is of less importance due to lower shear above the oscillatory boundary layer and hence we start to observe increasing importance of total transport that entrains turbulent kinetic energy from the lower oscillatory boundary layer to balance turbulent dissipation. The time rate of change in the TKE is also of more importance in this regime.

For $Ri = 1 \times 10^{-4}$, the TKE budget is similar to that of $Ri = 0$ within the oscillatory boundary layer (see figure 20 for $y = 0 \sim 12$). This is consistent with the results shown in figure 10 that the averaged velocity profiles for $Ri = 0$ and 1×10^{-4} are almost identical. The particle-induced buoyancy dissipation term is negligible in the TKE budget in this regime. On the other hand, the TKE budget becomes very different near the top and above the oscillatory boundary layer (see figure 19*b* for $y = 15 \sim 25$). Particle-induced buoyancy dissipation contributes to about 20 % to 50 % of the turbulent dissipation. Comparing to $Ri = 0$ (figure 19*a*), the overall intensities of these terms are smaller. Most noticeably, for a thickness extending from $y = 15$ upwards, the turbulent production for the $Ri = 1 \times 10^{-4}$ case is about 40 % to several factors smaller than that of $Ri = 0$. This thickness, Δy, is as small as 1 at $\phi = \pi/2$ and as large as 4.5 at $\phi = \pi/6$ which closely follows the depth of lutocline through the wave cycle. Also, between $y = 15 \sim 25$ the production term penetrates towards the mid-channel more than the case of $Ri = 0$. This reduction in the turbulence production explains the observed reduction in the turbulent fluctuation (see figure 11) and more importantly the formation of lutocline near the top of the oscillatory boundary layer. It is emphasized here that for the case of $Ri = 1 \times 10^{-4}$, because the region where turbulent production is significantly reduced is already of a very small magnitude compared with that near the bed, the total turbulence production in the entire domain is almost unchanged. Hence, the averaged velocity profiles for $Ri = 0$ and 1×10^{-4} are similar. Another observation on the production term is the change in the sign along the vertical direction when $Ri = 1 \times 10^{-4}$. For example, at the phases $\phi = \pi/6$ and $\phi = 5\pi/6$ between $y = 18$ to $y = 22$ negative production is observed. This is different from the production results for $Ri = 0$, where the production stays positive along the vertical direction at all the phases. This means the phase and the planar-averaged derivative of the mean flow along the vertical direction and the Reynolds stresses is of the same sign between $y = 18 \sim 22$ at the phases $\phi = \pi/6$ and $\phi = 5\pi/6$.

In the case of $Ri = 3 \times 10^{-4}$, a different picture in the TKE budget is observed (see figure 21) throughout the entire domain as compared with the other two cases.

https://doi.org/10.1017/S0022112010003769 Published online by Cambridge University Press

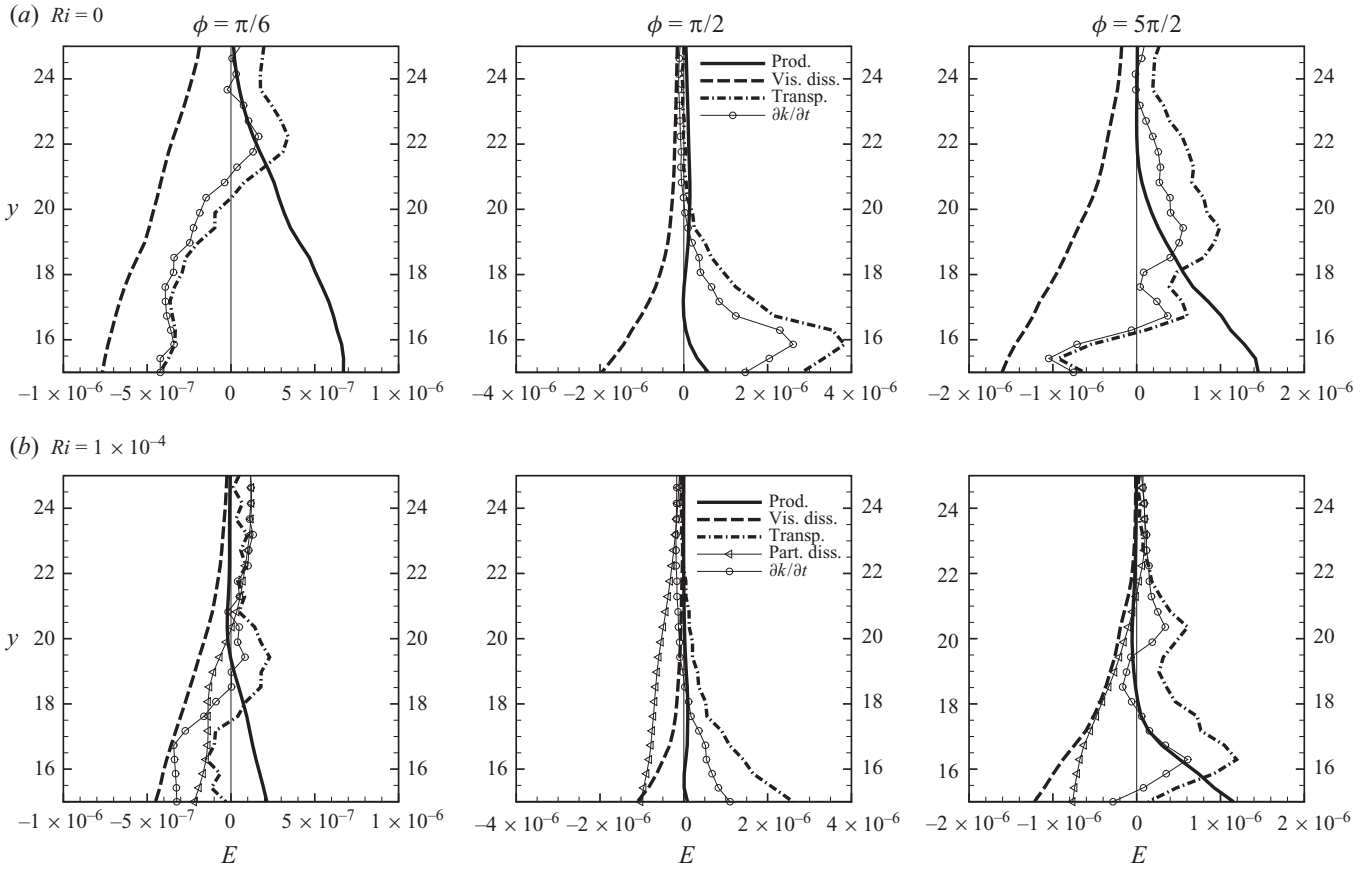

FIGURE 19. Profiles of the TKE budget terms for (*a*) $Ri = 0$ and (*b*) $Ri = 1 \times 10^{-4}$ at $y = 15 \sim 25$. Plotted are the turbulent production (Prod.), viscous dissipation (Vis. diss.), total kinetic energy transport (Total transp.), which is the sum of the diffusion, turbulent advection and pressure transport terms, and the time rate of change in the TKE ($\partial k/\partial t$).

https://doi.org/10.1017/S0022112010003769 Published online by Cambridge University Press

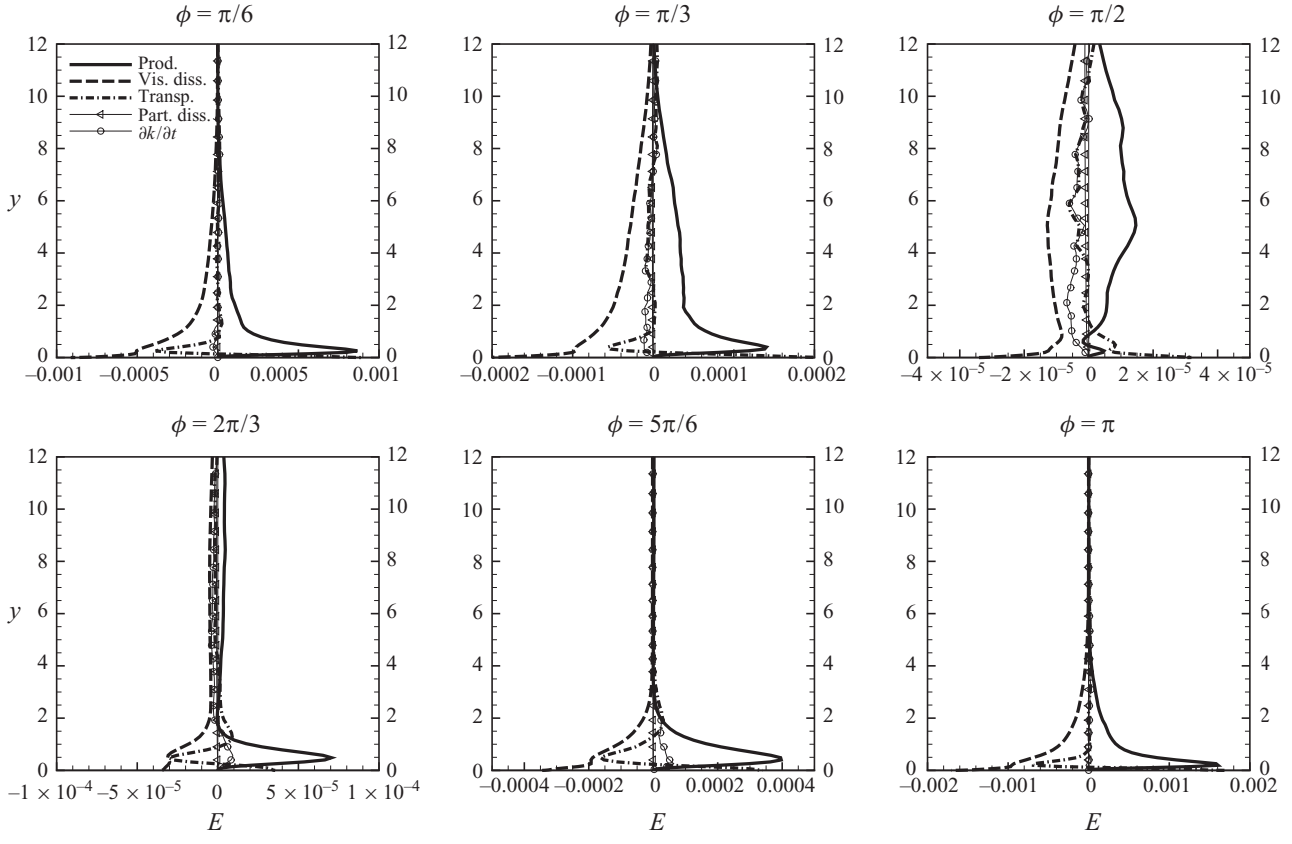

FIGURE 20. Profiles of the TKE budget terms for $Ri = 1 \times 10^{-4}$ at $y = 0 \sim 12$. Plotted are the turbulent production (Prod.), viscous dissipation (Vis. diss.), total kinetic energy transport (Total transp.), which is the sum of the diffusion, turbulent advection and pressure transport terms, dissipation due to particles (Partcle diss.) and the time rate of change in the TKE ($\partial k/\partial t$).

https://doi.org/10.1017/S0022112010003769 Published online by Cambridge University Press

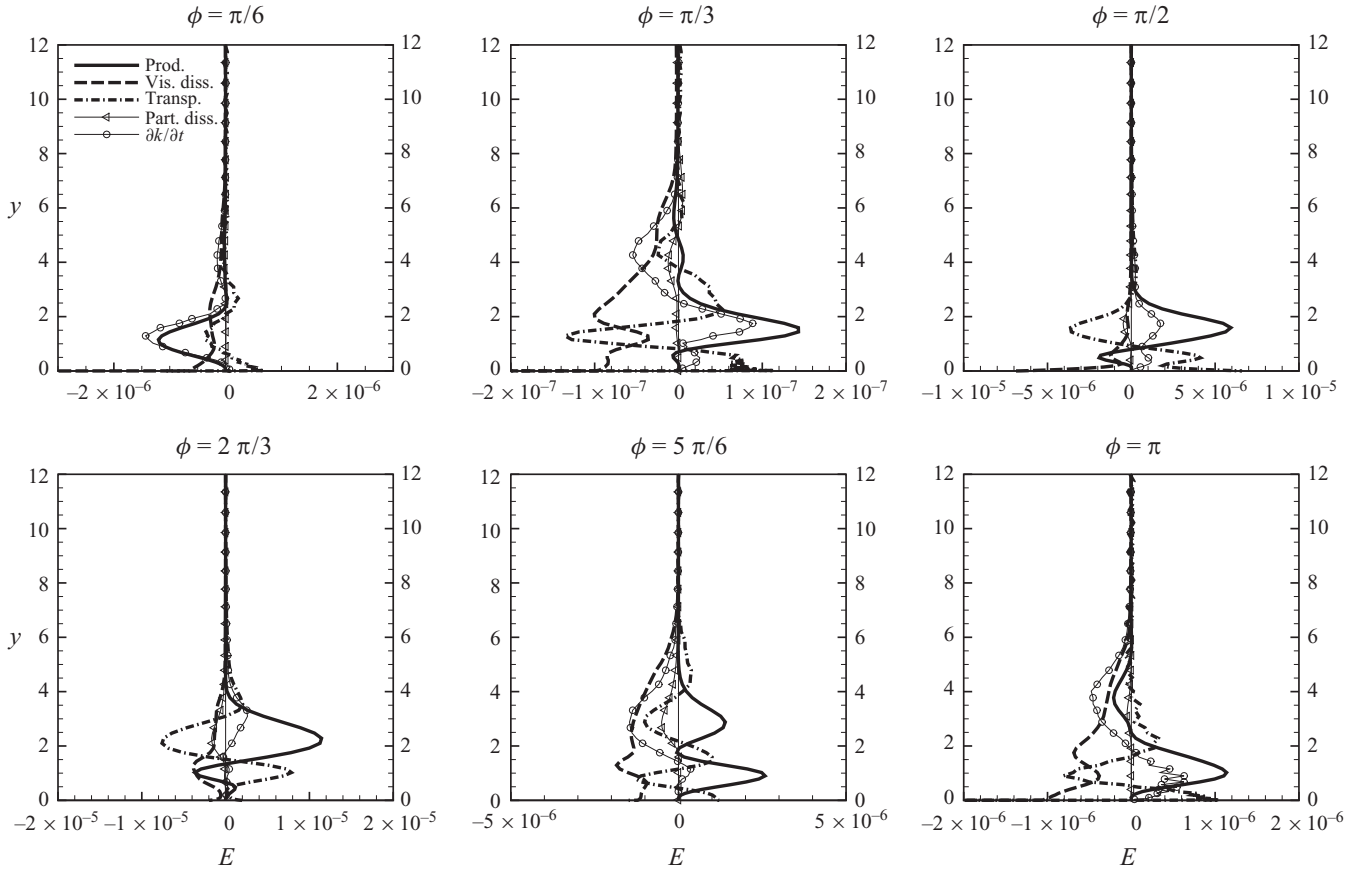

FIGURE 21. Profiles of the TKE budget terms for $Ri = 3 \times 10^{-4}$ at $y = 0 \sim 12$. Plotted are the turbulent production (Prod.), viscous dissipation (Vis. diss.), total kinetic energy transport (Total transp.), which is the sum of the diffusion, turbulent advection and pressure transport terms, dissipation due to particles (Particle diss.) and the time rate of change in the TKE ($\partial k/\partial t$).

First, the magnitudes of all terms in the TKE budget are significantly smaller at all the phases due to suppression of turbulence by strong particle-induced stable density stratification. However, at the onset of instability during the flow reversal ($\phi = \pi/2$), turbulent production is observed to occur around $y = 1 \sim 3$, which is consistent with the location of instability shown in figure 20. Because of such abrupt generation of turbulence, the time rate of change in the TKE and total transport become more important terms (than turbulent dissipation) to balance production. Such feature also triggers the upward particle burst observed during the flow instability. Note also that particle-induced buoyancy loss in the TKE becomes comparable to viscous dissipation with the onset of instability which falls between $\phi = \pi/2$ and $\phi = 2\pi/3$. Another observation is that peak dissipation due to particle buoyancy moves with the suspended particles in the vertical direction from the point where KH billows are first observed. Finally, because turbulent production is significantly reduced throughout the entire domain, the flow tends to laminarize (see averaged velocity shown in figure 10) and mixing is suppressed.

5. Flow regimes and field interpretations

Numerical simulations presented here qualitatively identify several regimes of fine-particle transport and their corresponding dynamics in an oscillatory channel flow. These regimes are consistent with prior laboratory and field studies on the fine-sediment transport in a wave boundary layer. Hence, this section provides a summary of flow regimes revealed by our numerical results and their field implications. It is illuminating here to convert, at least qualitatively, the bulk Richardson number (Ri) to the near-bed sediment mass concentration in the wave boundary layer. As mentioned, the present $Re_\Delta = 1000$ gives an amplitude of the oscillatory velocity of 0.56 m s^{-1} and the Stokes boundary layer thickness of 0.0018 m. Using Ri given in (2.8) and a sediment density of $\rho_p = 2650$ kg m^{-3}, the volume-averaged concentrations for the $Ri = 1 \times 10^{-4}$ and 3×10^{-4} cases can be deduced to be $\tilde{C} = 0.0011$ and 0.0033, respectively. The volume-averaged concentration is used to normalize the particle concentration in the calculations. Hence, according to the averaged concentration profiles presented in figure 9, the near-bed sediment mass concentration for $Ri = 1 \times 10^{-4}$ and 3×10^{-4} can be estimated to be $\tilde{C} = 10$ and 50 g l^{-1}, respectively.

According to the simulation results, we observe four flow regimes as the bulk Richardson number increases from the clear fluid condition ($Ri = 0$).

(i) Regime I describes a condition of very dilute sediment concentration (i.e. $Ri \to 0$, while $\tilde{C} \to 0$). The effect of sediment-induced density stratification is negligible and sediment is passive to the carrier flow. The sediment concentration profile is more or less well-mixed in and above the wave boundary layer. Simulation results suggest sediment concentration for this regime to be much smaller than 10 g l^{-1}. In fact, field observations identify such regime as low concentration mud suspension (e.g. Winterwerp & van Kesteren 2004) where the near-bed concentration is no more than $O(1)$ g l^{-1}.

(ii) Regime II describes a moderate interaction between the sediment and the carrier flow as the sediment concentration near the bed exceeds several grams per litre. Sediment-induced stable density stratification attenuates the carrier flow turbulence near the top of the wave boundary layer. Hence, the associated turbulent mixing of the sediment is significantly suppressed causing a pronounced 'shoulder-shape' concentration profile, characterized by a rapid decrease in the concentration near the top of the wave boundary layer. On the other hand, because the magnitudes

of turbulent production and turbulent kinetic energy around the top of the wave boundary layer are already small comparing with those within the wave boundary layer, the averaged flow velocity and turbulent intensity are only slightly modulated. The sharp gradient point in the concentration profile, called lutocline, exist not only for the fine-sediment suspension in the oscillating grid (Huppert *et al.* 1995), steady current or tidal flow (Trowbridge & Kineke 1994; Winterwerp 2001) but also observed in the field and laboratory during the wave-driven fine-sediment transport with a near-bed concentration of more than 10 g l^{-1} (e.g. Ross & Mehta 1989; Traykovski *et al.* 2000, 2007; Lamb, D'Asaro & Parsons 2004). Our simulation results are consistent with these observations on the wave-induced fluid mud transport.

(iii) In regime III, the near-bed sediment concentration is around several tens to 100 gl^{-1}, where strong coupling between the carrier flow and the sediment transport due to particle-induced density stratification is observed. Because of increasing effect of the stable sediment concentration gradient that directly suppresses turbulent production in the wave boundary layer, mean flow velocity tends to laminarize and causes a smaller wave boundary layer thickness. This feature of the carrier flow is quite different from that of regime II. Moreover, as the turbulent suspension of sediment in the wave boundary layer is shut down during a portion of the wave period, flow destabilizes during the flow reversal and episodic sediment bursts and increase in turbulence level occurs via flow instability. Subsequently, during the rest of the wave cycle the instability decays and a quiescent laminar flow is observed. From a comparison of the averaged velocity and concentration profiles with the laminar counterparts, we observe that they are nearly identical. It is not completely clear if such occurrence of instability during the flow reversal has been observed in the field or laboratory under the flow and sediment conditions considered in this study. Similarly, Foster, Beach & Holman (2006) observed that similar episodic near-bed sediment burst events occur only during the flow reversal in a sandy beach surf zone of 2 m flow depth. However, both the Reynolds number ($Re_{\Delta} \sim 2000$) and the non-dimensional settling velocity ($V_s = 2 \times 10^{-3}$) are about $2-3$ times larger than the conditions considered in this study. One might argue that the larger Reynolds number contributes to enhanced turbulence and as a result a larger particle settling velocity (or larger concentration) is required to establish the condition of instability during the flow reversal. The effect of increased particle settling velocity at a fixed bulk Richardson number on turbulent suppression and laminarization has been discussed by Cantero *et al.* (2009*a*) and Cantero, Balachandar & Parker (2009*b*) in the context of turbidity currents. Conley & Inman (1992) report field observations on sandy beaches under near-breaking waves. They measure intense sand suspension events, characterized by the development of rolling and pluming regimes, only during the passage of a wave crest. It is noted here that the wave shape in the study of Conley & Inman (1992) is quite skewed (e.g. velocity amplitude is significantly larger during the wave crest) and the grain size is considerably larger (~ 150 μm in diameter) than that considered in this study. P. Traykovski (personal communication, 2009) has observed lutocline waves during wave-driven fluid mud events. These lutocline waves had wavelengths much smaller than the surface wavelength. However, the near-bed sediment concentration observed is of a few hundred grams per litre and hence the measured lutocline wave may be mostly controlled by rheological stresses and associated non-Newtonian flow effects, which are not incorporated in this study.

(iv) In regime IV, where the near-bed sediment concentration is greater than $O(100)$ gl^{-1}, sediment-induced stable density stratification is severe enough that it

further suppresses the instability observed in regime III and the flow remains laminar at all times. Complete laminarization of the turbulent wave boundary layer due to sediment-induced stable density stratification has been hypothesized in many models to study wave dissipation over a muddy seabed. In such study, the wave boundary layer is calculated based on a laminar formulation with an enhanced effective viscosity or non-Newtonian (e.g. Bingham-plastic) viscosity that further damps the wave energy (e.g. Dalrymple & Liu 1978; Mei & Liu 1987). Our simulation results discussed here support such a laminar flow assumption. In a laboratory study of fine sediment transport in an oscillatory tunnel, Lamb *et al.* (2004) report that as the wave velocity amplitude increases, wave boundary layer thickness also increases and more sediment is suspended from the bed. However, a critical wave velocity amplitude seems to exist such that when the wave amplitude is further increased, the wave boundary layer turbulence eventually collapses and the wave boundary layer thickness decreases. This observation of the carrier flow behaviour is consistent with our simulation results shown here.

In many coastal modelling applications, the effects of wave boundary layer are parameterized by a friction factor (or by a drag coefficient). It is well known that when the presence of sediment attenuates the carrier flow turbulence, the friction factor experienced by overlaying hydrodynamics is reduced (e.g. Glenn & Grant 1987; Styles & Glenn 2000). Our simulation results suggest such a paradigm for fine sediment may need to be refined for the wave-induced fine sediment transport. Sediment-induced stable density stratification affects sediment suspension and carrier flow in wave boundary layer in two different levels. For a milder concentration, there exists a regime (regime II) of weak turbulence attenuation where sediment mixing is suppressed only at the top of the wave boundary layer to form a lutocline. However, the mean flow field is intact and hence there is no need to revise the friction factor associated with the mean flow energy dissipation. Only at higher concentration, such as regimes III and IV, is turbulence significantly attenuated and friction factor must be reduced. In most field studies on wave propagation over a muddy seabed (e.g. Forristal & Reece 1985; Sheremet & Stone 2003; Elgar & Raubenheimer 2008), there are mostly reports on increased energy dissipation due to the presence of mud in the wave boundary layer instead of drag reduction. Our simulation results here imply the presence of a lower concentration of the fluid mud may not reduce the friction factor (e.g. regime II). As the sediment concentration further increases such that sediment-induced stable density stratification directly reduces turbulent production, the mean flow laminarizes. In the meantime, rheological stress may further become effective due to high sediment concentration to attenuate wave energy. Hence, it is likely that the range of the sediment concentration in the wave boundary layer that attenuates turbulence and causes reduction of friction is limited.

6. Conclusions

Highly accurate numerical simulations have been carried out for fine-particle transport in an oscillatory boundary layer. Two-way coupled simulations adopting a simplified Eulerian–Eulerian model are used to simplify particle phase formulation appropriate for the small particle response time. In this study, we further neglect higher-order particle inertia terms and the resulting turbulence modulation is only due to particle-induced density stratification. Flow turbulence is fully resolved at a Reynolds number of $Re_\Delta = 1000$. We present four cases with a non-dimensional particle settling velocity of $V_s = 9 \times 10^{-4}$ at different bulk Richardson numbers,

i.e. $Ri = 0, 1 \times 10^{-4}$, 3×10^{-4} and 6×10^{-4}, representing various degrees of particle-induced stable density stratification.

At $Ri = 1 \times 10^{-4}$, which corresponds to a near-bed sediment concentration of 10 g l^{-1} for the Reynolds number and settling velocity selected, sediment-induced stable density stratification attenuates flow turbulence and reduces mixing of the sediment near the top of the wave boundary layer, which gives the formation of a sharp concentration gradient, i.e. lutocline. This test case also gives a qualitative estimate on the minimum concentration for which particle cannot be considered as passive to the carrier flow turbulence. On the other hand, turbulence near the bed is not affected by the sediment and the mean flow velocity is almost identical to the clear fluid condition. At $Ri = 3 \times 10^{-4}$ (near-bed concentration about 50 g l^{-1}), particle-induced density stratification is strong enough to attenuate turbulence in the entire wave boundary layer. The flow tends to be laminarized and the mean flow velocity and concentration profiles become similar to the laminar solution. However, flow instability, which can be clearly seen both in the coherent vortical structure and instantaneous particle concentration, occurs during the flow reversal which triggers large fluctuation production and particle suspension that last about one-third of the wave period. Finally, at $Ri = 6 \times 10^{-4}$ (near-bed concentration more than 100 g l^{-1}), an oscillatory boundary layer flow becomes completely laminarized at all times due to intense sediment-induced stable density stratification.

At $Ri = 3 \times 10^{-4}$ or greater, turbulence is attenuated across the entire oscillatory boundary layer and hence the oscillatory boundary layer thickness and friction are reduced due to particle-induced stable density stratification. In most cohesive sediment transport studies, when sediment concentration is greater than $O(100)$ g l^{-1}, rheological stresses caused by interactions among the floc aggregates and interstitial water need to be considered. Rheological stress gives an enhanced effective viscosity that can further increase energy dissipation and friction factor. These non-Newtonian flow features shall be studied in the future work. This study identifies several distinct regimes of the particle-laden oscillatory boundary layer according to different magnitudes of the bulk Richardson number (or sediment concentration). Although the exact value of Ri for these regimes must depend on the Reynolds number and the settling velocity, the characteristics of these regimes are useful to explain the wave-driven cohesive sediment transport process in coastal environments. Future work shall be devoted to explore these characteristics for different settling velocity and Reynolds number. Finally, more detailed laboratory and field measurements shall be carried out to verify several interesting observations revealed by the present numerical simulations, such as flow instability that occurs during the flow reversal.

This study is supported by the US Office of Naval Research (N00014-09-1-0134) and National Science Foundation (OCE-0913283; OCE-0926974) to the University of Delaware and by the US Office of Naval Research grant (N00014-07-1-0494) to the University of Florida. This work is partially supported by the National Center for Supercomputing Applications under OCE70005N and OCE80005P utilizing the NCSA Cobalt and PSC Pople. Also, the authors acknowledge the University of Florida High-Performance Computing Center for providing computational resources and support that have contributed to the research results reported in this paper.

REFERENCES

Akhavan, R., Kamm, R. D. & Shapiro, A. H. 1991 An investigation of transition to turbulence in bounded oscillatory Stokes flows. Part 2: Numerical simulations. *J. Fluid Mech.* **225**, 423–444.

Armenio, V. & Sarkar, S. 2002 An investigation of stably stratified turbulent channel flow using large-eddy simulation *J. Fluid Mech.* **459**, 1–42.

Bagchi, P. & Balachandar, S. 2003 Effect of turbulence on the drag and lift of a particle. *Phys. Fluids* **15** (3), 496–513.

Bagchi, P. & Balachandar, S. 2004 Response of the wake of an isolated particle to an isotropic turbulent flow. *J. Fluid Mech.* **518**, 95–123.

Balachandar, S. & Eaton, J. K. 2010 Turbulent dispersed multiphase flow. *Annu. Rev. Fluid Mech.* **42**, 111–133.

Barenblatt, G. F. 1953 On the motion of suspended particles in a turbulent stream. *Prikladnaja Mat. Mekh. Engl. Trans.* **17**, 261–274.

Birman, V., Martin, J. E. & Meiburg, E. 2005 The non-Boussinesq lock–exchange problem. Part 2: High-resolution simulations. *J. Fluid Mech.* **537**, 125–144.

Blennerhassett, P. J. & Bossom, A. P. 2002 The linear stability of flat Stokes layers. *J. Fluid Mech.* **464**, 393–410.

Blennerhassett, P. J. & Bossom, A. P. 2006 The linear stability of high-frequency oscillatory flow in a channel. *J. Fluid Mech.* **556**, 1–25.

Bonometti, T. & Balachandar, S. 2008 Effect of Schmidt number on the structure and propagation of density currents. *Theor. Comput. Fluid Dyn.* **22**, 341–361.

Burton, T. M. & Eaton, J. K. 2005 Fully resolved simulations of particle–turbulence interaction. *J. Fluid Mech.* **545**, 67–111.

Cantero, M. I., Balachandar, S., Cantelli, A., Pirmez, C. & Parker, G. 2009*a* Turbidity current with a roof: direct numerical simulation of self-stratified turbulent channel flow driven by suspended sediment. *J. Geophys. Res.* **114**, C03008.

Cantero, M. I., Balachandar, S. & Garcia, M. 2008 An Eulerian–Eulerian model for gravity currents driven by inertial particles. *Intl J. Multiph. Flow* **34**, 484–501.

Cantero, M. I., Balachandar, S. & Parker, G. 2009*b* Direct numerical simulation of stratification effects in a sediment-laden turbulent channel flow. *J. Turbulence* **10**, 1–28.

Canuto, C., Hussaini, M. Y., Quarteroni, A. & Zang, T. A. 1987 *Spectral Methods in Fluid Dynamics*. Springer.

Chakraborty, P., Balachandar, S. & Adrian, R. J. 2005 On the relationships between local vortex identification schemes. *J. Fluid Mech.* **535**, 189–214.

Chang Y. S. & Scotti, A. 2006 Turbulent convection of suspended sediments due to flow reversal. *J. Geophys. Res.* **111** (C07001), doi:10.1029/2005JC003240.

Conley, D. C., Falchetti, S., Lohmann, I. P. & Brocchini, M. 2008 The effects of flow stratification by non-cohesive sediment on transport in high-energy wave-driven flows. *J. Fluid Mech.* **610**, 43–67.

Conley, D. S. & Inman, D. L. 1992 Field observations of the fluid-granular boundary layer under near breaking waves. *J. Geophys. Res.* **97**, C6, 9631–9643.

Cortese, T. & Balachandar, S. 1995 High performance spectral simulation of turbulent flows in massively parallel machines with distributed memory. *Intl J. Supercomput. Appl.* **9** (3), 187–204.

Costamagna, P., Vittori, G. & Blondeaux, P. 2003 Coherent structures in oscillatory boundary layers. *J. Fluid Mech.* **474**, 1–33.

Dalrymple, R. A. & Liu, P. L. 1978 Waves over soft mud beds: a two-layer fluid mud model. *J. Phys. Oceanogr.* **8**, 1121–1131.

Einstein, H. A. & Chien, N. 1955 Effects of heavy sediment concentration near the bed on velocity and sediment distribution. MRD Sediment Ser. 8, University of California, Berkeley.

Elgar, S. & Raubenheimer, B. 2008 Wave dissipation by muddy seafloors. *Geophys. Res. Lett.* **35** (L07611), doi:10.1029/2008GL033245.

Elgobashi, S. 1991 Particle-laden turbulent flows: direct simulation and closure models. *Appl. Sci. Res.* **52**, 301–314.

Elgobashi, S. & Truesdell, G. C. 1992 Direct simulation of particle dispersion in a decaying isotropic turbulence. *J. Fluid Mech.* **242**, 655–700.

Elgobashi, S. & Truesdell, G. C. 1993 On the 2-way interaction between homogeneous turbulence and dispersed solid particles. Part 1: Turbulence modification. *Phys. Fluids* A **5**, 1790–1801.

Felix, M. 2002 Flow structure of turbidity currents. *Sedimentology* **49**, 397–419.

Forristall, G. Z. & Reece, A. M. 1985 Measurements of wave attenuation due to a soft bottom: the SWAMP experiment. *J. Geophys. Res.* **90**, 3367–3380.

Foster, D. L., Beach, R. A. & Holman, R. A. 2006 Turbulence observations of the nearshore wave bottom boundary layer. *J. Geophy. Res.* **111** (C04011).

Gelfenbaum, G. & Smith, J. D. 1986 Experimental evaluation of a generalized suspended-sediment transport theory. In *Shelf Sands and Sand Stones* (ed. R. J. Knight & J. R. McLean), pp. 133–144, Canadian Society of Petroleum Engineers.

Glenn, S. M. & Grant, W. D. 1987 A suspended sediment stratification correction for combined wave and current flows. *J. Geophys. Res.* **92** (C8), 8244–8264.

Hall, P. 1978 The linear stability of flat Stokes layers. *Proc. R. Soc. Lond.* A **359**, 151–166.

Hall, B., Meiburg, E. & Kneller, B. 2008 Channel formation by turbidity currents: Navier–Stokes based linear stability analysis. *J. Fluid Mech.* **615**, 185–210.

Harris, T. C., Hogg, A. J. & Huppert, H. E. 2001 A mathematical framework for the analysis of particle-driven gravity currents. *Proc. R. Soc. Lond.* A **457**, 1241–1272.

Harris, C. K., Traykovski, P. A. & Geyer, W. R. 2005 Flood dispersal and deposition by near-bed gravitational sediment flows and oceanographic transport: a numerical modeling study of the Eel River shelf, northern California. *J. Geophys. Res.* **110**, C09025, doi:10.10292004JC002727.

Hino, M. 1963 Turbulent flow with suspended particles. *J. Hydraul. Div. Am. Soc. Civ. Engng* **89** (HY4), 161–185.

Hino, M., Kashiwayanagi, M., Nakayama, A. & Hara, T. 1983 Experiments on the turbulence statistics and the structure of a reciprocating oscillatory flow. *J. Fluid Mech.* **131**, 363–400.

Hino, M., Sawamoto, M. & Takasu, S. 1976 Experiments on transition to turbulence in an oscillatory pipe flow. *J. Fluid Mech.* **75**, 193–207.

Howard, L. N. 1961 Note on a paper by John W. Miles. *J. Fluid Mech.* **10**, 509–512.

Hsu, T.-J., Jenkins, J. T. & Liu, P. L.-F. 2004 On two-phase sediment transport: sheet flow of massive particles. *Proc. R.. Soc. Lond.* A **460** (2048), 2223–2250.

Hsu, T.-J., Ozdemir, C. E. & Traykovski, P. A. 2009 High resolution numerical modeling of wave-supported sediment gravity-driven mudflows. *J. Geophys. Res.* **114**, C05014, doi:10.1029/2008JC005006.

Hsu, T.-J., Traykovski, P. A. & Kineke, G. C. 2007 On modeling boundary layer and gravity driven fluid mud transport. *J. Geophys. Res.* **112**, C04011, doi:10.1029/2006JC003719.

Huppert, H. E., Turner, J. S. & Hallworth, M. A. 1995 Sedimentation and entrainment in dense layers of suspended particles stirred by an oscillating-grid. *J. Fluid Mech.* **289**, 263–293.

Ivey, G. N. & Imberger, J. 1991 On the nature of turbulence in a stratified fluid. Part 1: The energetics of mixing. *J. Phys. Oceanogr.* **21**, 650–658.

Jensen, B. L., Sumer, M. & Fredsóe J. 1989 Turbulent oscillatory boundary layers at high Reynolds numbers. *J. Fluid Mech.* **206**, 265–297.

Lamb, M. P., D'Asaro, E. & Parsons, J. D. 2004 Turbulent structure of high-density suspensions formed under waves. *J. Geophys. Res.* **109**, C12026.

Maxey, M. R. 1987 The gravitational settling of aerosol particles in homogeneous turbulence and random flow fields. *J. Fluid Mech.* **174**, 441–465.

McLaughlin, J. B. 1989 Aerosol particle deposition in numerically simulated channel flow. *Phys. Fluids* A **1**, 1211–1224.

Mei, C. C. & Liu, K. F. 1987 A Bingham plastic model for a muddy seabed under long waves. *J. Geophys. Res.* **94** (C13) 14 581–14 594.

Miles, J. W. 1961 On the stability of heterogeneous shear flows. *J. Fluid Mech.* **10**, 496–508.

Necker, F., Hartel, C., Kleiser, L. & Meiburg, E. 2002 High-resolution simulations of particle-driven gravity currents. *Intl J. Multiph. Flow* **29**, 279–300.

Noh, Y. & Fernando, J. S. 1991 Dispersion of suspended particles in turbulent flow. *Phys. Fluids* A **3**(7), 1730–1740.

Nowak, N., Kakade, P. P. & Annapragada, A. V. 2003. Computational fluid dynamics simulation of airflow and aerosol deposition in human lungs. *Ann. Biomed. Engng* **31**, 374–390.

Ozdemir, C. E., Hsu, T.-J. & Balachandar, S. 2010 Simulation of fine sediment transport in oscillatory boundary layer. *J. HydroEnviron. Res.* **3**, 247–259.

Rogers, C. B. & Eaton, J. K. 1991 The effect of small particles on fluid turbulence in a flat-plate, turbulent boundary layer in air. *Phys. Fluids* A **3**, 928–937.

Ross, M. A. & Mehta, A. J. 1989 On the mechanics of lutoclines and fluid muds. *J. Coastal. Res.* **5**, 51–61.

Salon, S., Armenio, V. & Crise, A. 2007 A numerical investigation of the Stokes boundary layer in the turbulent regime. *J. Fluid Mech.* **570**, 253–296.

Sarpkaya, T. 1993 Coherent structures in oscillatory boundary layers. *J. Fluid Mech.* **253**, 105–140.

Schumann, U. & Gerz, T. 1995 Turbulent mixing in stably stratified shear flows. *J. Appl. Meteor.* **34**, 33–48.

Scotti. A. & Piomelli, U. 2001 Numerical simulation of pulsating turbulent channel flow. *Phys. Fluids* **13** (5), 1367–1384.

Sequeiros, O. E., Cantelli, A., Viparelli, E., White, J. D. L., Garcia, M. H. & Parker, G. 2009 Modeling turbidity currents with non-uniform sediment and reverse buoyancy. *Water Resour. Res.* **45**, W06408.

Sheremet, A. & Stone, G. W. 2003 Observations of nearshore wave dissipation over muddy sea beds. *J. Geophys. Res.* **108** (C11), 3357.

Spalart, P. R. & Baldwin, B. S. 1989 Direct simulation of a turbulent oscillating boundary layer. In *Turbulent Shear Flows 6* (ed. J. C. Andre), pp. 417–440, Springer.

Squires, K. D. & Eaton, J. K. 1991 Preferential concentration of particles by turbulence. *Phys. Fluids* A **3**, 1169.

Strang, E. J. & Fernando, H. J. S. 2001 Entrainment and mixing in stratified shear flows. *J. Fluid Mech.* **428**, 349–386.

Styles, R. & Glenn, S. M. 2000 Modeling stratified wave and current bottom boundary layers in the continental shelf. *J. Geophys. Res.* **105**, 24119–24139.

Tanaka, T. & Eaton, J. K. 2008 Classification of turbulence modification by dispersed spheres using a novel dimensionless number. *Phys. Rev. Lett.* **101**, 114502.

Taylor, G. I. 1931 Effect of variation in density on the stability of superposed streams of fluid. *Proc. R. Soc. Lond.* A **132**, 499–523.

Taylor, M. G. 1959 The influence of the anomalous viscosity of blood upon its oscillatory flow. *Phys. Med. Biol.* **3**, 273–290.

Traykovski, P., Geyer, W. R., Irish, J. D. & Lynch, J. F. 2000 The role of wave-induced fluid mud flows for cross-shelf transport on the Eel River continental shelf. *Cont. Shelf Res.* **20**, 2113–2140.

Trowbridge, J. H. & Kineke, G. C. 1994 Structure and dynamics of fluid mud on the Amazon continental shelf. *J. Geophys. Res.* **99** (C1), 865–874.

Turner, J. S. 1973 *Buoyancy Effects in Fluids*. Cambridge University Press.

Vanoni, V. A. 1946 Transportation of suspended sediment by water. *ASCE Trans.* **111**, 67–133.

Vittori, G. & Verzicco, R. 1998 Direct simulation of transition in an oscillatory boundary layer. *J. Fluid Mech.* **371**, 207–232.

Winterwerp, J. C. 2001 Stratification effects by cohesive and non-cohesive sediment. *J. Geophys. Res.* **106** (C10), 22559–22574.

Winterwerp, J. C. 2002 On the flocculation and settling velocity of estuarine mud. *Cont. Shelf Res.* **22**, 1339–1360.

Winterwerp, J. C. & Van Kesteren, W. G. M. 2004 *Introduction to the Physics of Cohesive Sediment in the Marine Environment*. Elsevier.

Yang, J. N., Chung, T. R., Troutt, & Crowe, C. T. 1990 The influence of particles on the spatial stability of two-phase mixing layers. *Phys. Fluids* A **2**, 1839.

Yu, X, Hsu, T.-J. & Hanes, D. M. 2010 Sediment transport under wave groups: the relative importance between wave shape and boundary layer streaming. *J. Geophys. Res.* **15**, C02013, doi:10.1029/2009JC005348.

Zeng, L., Balachandar, S., Fischer, P. & Najjar, F. M. 2008 Interactions of a stationary finite-sized particle with wall turbulence. *J. Fluid Mech.* **594**, 271–305.

Zeng, L., Balachandar, S. & Najjar, F. M. 2010 Wake response of a stationary finite-sized particle in a turbulent channel flow. *Intl J. Multiph. Flow* **36**, 406–422.

Zhou, D. & Ni, J. R. 1995 Effects of dynamic interaction on sediment laden turbulent flows. *J. Geophys. Res.* **100** (C1), 981–996.

Zhou, J., Adrian, R. J., Balachandar, S. & Kendall, T. M. 1999 Mechanisms for generating coherent packets of hairpin vortices in channel flow. *J. Fluid Mech.* **387**, 353–396.